solar

Review

Advances on Sb_2Se_3 Solar Cells Fabricated by Physical Vapor Deposition Techniques

Roberto Jakomin, Stefano Rampino, Giulia Spaggiari and Francesco Pattini

Topic
Photovoltaic Materials and Devices

Edited by
Prof. Dr. Bin Yang, Prof. Dr. Yongbo Yuan and Dr. Salvatore Lombardo

MDPI

https://doi.org/10.3390/solar3040031

solar

MDPI

Review

Advances on Sb_2Se_3 Solar Cells Fabricated by Physical Vapor Deposition Techniques

Roberto Jakomin [1], Stefano Rampino [2,*], Giulia Spaggiari [2,3] and Francesco Pattini [2]

[1] Campus Duque de Caxias, Universidade Federal do Rio de Janeiro, Rio de Janeiro 25240-005, Brazil; robertojakomin@xerem.ufrj.br
[2] Consiglio Nazionale delle Ricerche, IMEM Institute, 43124 Parma, Italy; giulia.spaggiari1@unipr.it (G.S.); francesco.pattini@cnr.it (F.P.)
[3] Department of Mathematical, Physical and Computer Sciences, University of Parma, Parco Area delle Scienze 7/a (Campus), 43124 Parma, Italy
* Correspondence: stefano.rampino@cnr.it

Abstract: Sb_2Se_3, as an earth-abundant and low-toxic material, has emerged as one of the most interesting absorbers for clean renewable power generation technologies. Due to its optical properties, especially bandgap and absorption coefficient, the number of papers on Sb_2Se_3-based solar cells has been constantly increasing in the last ten years, and its power conversion efficiency has raised from 1% in 2014 to 10.57% in 2022. In this review, different Sb_2Se_3 solar cells' fabrication technologies based on physical vapor deposition are described and correlated to the texture coefficient (ribbon orientation). Moreover, recent research works of the most promising solar cell configurations with different electron-transporting layers and hole-transporting layers are analyzed with a special emphasis on photovoltaic performances. Furthermore, different Sb_2Se_3 doping techniques are discussed. All these aspects are considered as new strategies to overcome the Sb_2Se_3 solar cell's actual limitations.

Keywords: Sb_2Se_3; solar cells; physical vapor deposition; chalcogenides

Citation: Jakomin, R.; Rampino, S.; Spaggiari, G.; Pattini, F. Advances on Sb_2Se_3 Solar Cells Fabricated by Physical Vapor Deposition Techniques. *Solar* **2023**, *3*, 566–595. https://doi.org/10.3390/solar3040031

Academic Editor: Dongsheng Li

Received: 3 August 2023
Revised: 18 September 2023
Accepted: 28 September 2023
Published: 12 October 2023

1. Introduction

Thin-film solar cells are the most promising alternative to crystalline silicon solar cells because they use less material, are less expensive, and can be integrated into flexible devices. Chalcogenide thin-film solar cells, especially those based on CdTe and Cu(In,Ga)Se2, are the most dominant in the thin-film photovoltaic market due to their good stability and efficiency (22.1% for CdTe and 23.35% for CIGS) [1]. Perovskite solar cells have also achieved high efficiencies up to 23.7% in recent years, but they are still not reliable enough for mass production.

Silicon (Si)-based solar cells are the dominant technology in the photovoltaic (PV) market. They have a high power-to-cost ratio due to their high efficiency (up to 26.7%) and the fact that silicon is abundant on Earth. However, the production of single-crystal silicon wafers is energy-intensive, and silicon must be more than 100 µm thick to absorb enough sunlight [2]. Chalcogenide materials, on the other hand, have a high optical absorption coefficient, which allows them to be made into lighter and more flexible panels, and they also have lower material and energy production costs.

Among chalcogenides, antimony selenide (Sb_2Se_3) has attracted attention as a potential absorber material for thin-film solar cells due to its excellent optical (very high absorption coefficient $>10^5$ cm^{-1}) and electrical (p-type conductivity between 10^{-7} S/cm and 4.6×10^2 S/cm) properties. It is also a binary semiconductor with a low melting point of 608 °C.

Furthermore, the scarcity of indium and the toxicity of cadmium have led to increased interest in this type of material, which is made from abundant elements such as Se, Sb, and S that are not considered to be highly toxic or carcinogenic.

Another interesting feature of Sb_2Se_3 is that there is still a lot of room for improvement in its research. In fact, with its 1.2 eV band gap [3], the Shockley–Queisser theory predicts a theoretical power conversion efficiency (PCE) of 31.7% [4]. The highest experimental efficiency achieved so far is 10.57% [5]. In comparison, silicon solar cells have been developed for over 70 years and have reached their efficiency limit. In contrast, Sb_2Se_3 solar cells have rapidly increased their efficiency from 1% to 10.57% in less than 10 years.

Sb_2Se_3 forms one-dimensional ribbons along the c-axis through Sb–Se covalent bonds [6]. The ribbons are stacked together in the perpendicular directions by weaker van der Waals forces [7].

The quasi-one-dimensional structure of Sb_2Se_3 induces strong anisotropic properties, especially for electrical conductivity. The carrier mobility of the ribbons oriented along the (001) growth direction is higher than along other directions.

This is because surfaces parallel to the (001) direction, such as (110) and (120) surfaces, have no dangling bonds and consequently lead to reduced nonradiative recombination losses [6].

In particular, the hole mobility along the ribbons is high (45 cm^2/Vs at 300 K), while the carrier transport perpendicular to the covalent bond directions is much smaller because it is associated with a hopping conduction mechanism [8].

In order to maximize the efficiency of Sb_2Se_3 solar cells, it is important to align the ribbons closer to the growth direction (perpendicular to the substrate), such as the (211) and (221) crystal orientations. It is also important to minimize the grain orientation along the (hk0) directions.

The low experimental efficiency of Sb_2Se_3 solar cells is mainly due to the following factors:

- Short carrier lifetime: The carrier lifetime is the average time that a charge carrier (electron or hole) can exist before it recombines with another carrier. The short carrier lifetime in Sb_2Se_3 is due to the high density of defects, such as Se vacancies and Sb_{Se}/Se_{Sb} antisite defects [9].
- Low hole density: The hole density is the number of holes per unit volume in a semiconductor material. The low hole density in intrinsic Sb_2Se_3 is another factor that limits the efficiency of the solar cells [2].
- Lack of suitable hole and electron transport layer materials: The hole transport layer (HTL) and electron transport layer (ETL) are the materials that transport the holes and electrons, respectively, to the respective electrodes of the solar cell. The lack of suitable HTL and ETL materials is also a challenge for the development of high-efficiency Sb_2Se_3 solar cells [10].

In order to reduce interface/surface defects, strategies such as defect passivation have been explored. Defect passivation is the process of covering the defects with a material that will prevent them from recombining with charge carriers. This can be done by selenizing the surface of the Sb_2Se_3 or by covering it with a passivating layer [11].

The band alignment between the electron transport layer (ETL) and hole transport layer (HTL) and Sb_2Se_3 is not ideal, which causes an inefficient extraction and transport of photocarriers at the interface with the absorber.

The commonly used ETLs include CdS, TiO_2, ZnO, and SnO_2. The HTLs that have been reported in the literature are organic, such as spiro-OMeTAD, P3HT, PCDTBT, and CZ-TA, or inorganic, such as NiO_x, CuSCN, and $CuSbSe_2$ [12].

In the past few years, several studies have been published on the deposition of Sb_2Se_3 thin films for solar cells. One common method is the spin-coating deposition on mesoporous oxides in dye-sensitized solar cells (DSSC) structures [13]. This method is simple and scalable, but it can be difficult to control the thickness and uniformity of the film.

Another common method is to deposit Sb_2Se_3 from the vapor phase. This can be done using a variety of technique: these methods can produce high-quality films with a good control over thickness and uniformity.

Recently, close-spaced sublimation (CSS) and injection vapor deposition (IVD) have demonstrated power conversion efficiencies (PCE) of 9.2% (in 2019) and 10.12% (in 2022), respectively. The record of 10.57% (in 2022) was achieved using additive-assisted chemical bath deposition (CBD) [5]. Although the number of laboratories involved in Sb_2Se_3 research is still small, the improvements in cell efficiency have been even faster than those achieved in CIGS and CZTS technologies in their first 10 years of research (Figure 1) [14].

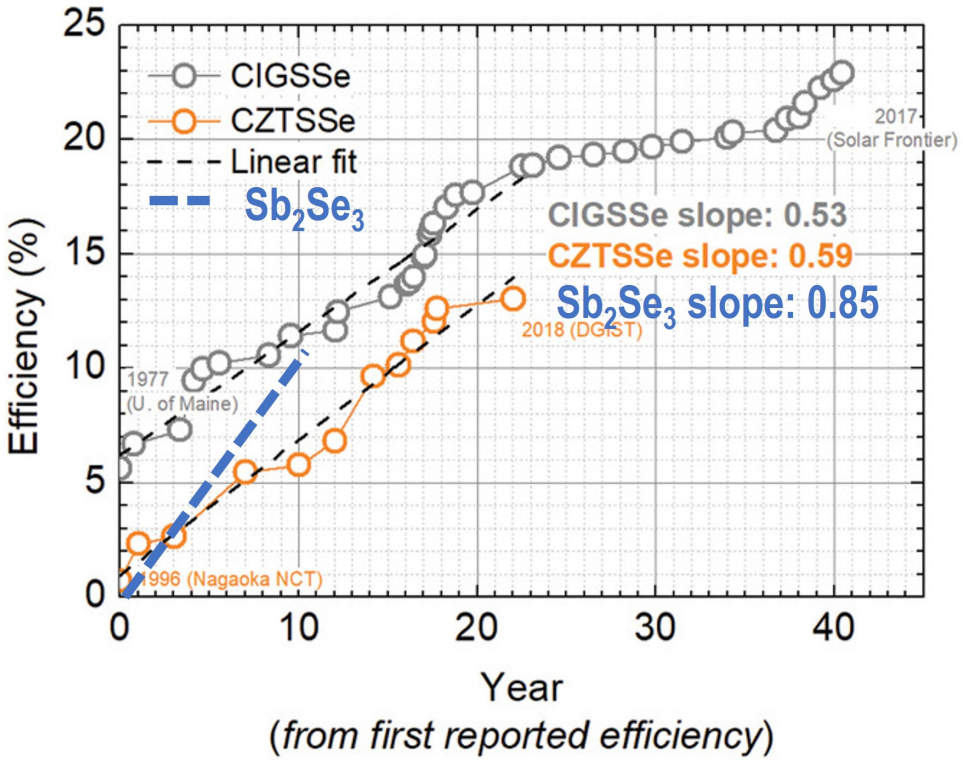

Figure 1. Record efficiencies versus time for Sb_2Se_3-, CIGSSe-, and CZTSSe-based solar cells. Year 0 is 1977 for CIGSSe [15], 1997 for kesterites [16], 2013 for Sb_2Se_3. Adapted with permission from [14] Copyright © 2019, John Wiley and Sons.

Although significant progress has been made in increasing the efficiency of Sb_2Se_3 solar cells, many challenges remain, such as surface/interface recombination, effective doping, and optimal HTL/absorber/ETL band alignment.

The photocarrier mobility is strongly dependent on the grain orientation, so controlling the ribbon orientation is one of the most important goals for Sb_2Se_3 absorbers in photovoltaic applications. The texture coefficient is hence a fundamental parameter for evaluating the potential of different deposition methods. However, although many studies have reported their texture coefficients, the relative values are rarely calculated, making it difficult to directly compare the obtained absorbers.

This paper reviews recent advances in Sb_2Se_3 solar cells fabricated in planar configuration using physical deposition techniques (PDT). The different relative texture coefficients (TCs) have been extrapolated from the available literature data, which allows for the comparison of ribbon alignment for different deposition methods and structures, and their correlation with the main solar cell performance. The different ETL/absorber/HTL solar cell architectures are then discussed, especially considering their band alignment strategies for enhancing photovoltaic performance. Finally, the different doping strategies for Sb_2Se_3-based absorbers are summarized, evaluating the achieved carrier transport properties and the reported solar cell efficiencies.

The paper is divided into four sections. Section 2 describes the different physical deposition techniques (PDTs) used to fabricate Sb_2Se_3 solar cells. Section 3.1 correlates

the PDTs and cell configurations with the ribbon orientation. Section 3.2 discusses the different HTL/ETL, interfacial engineering, and band alignment strategies that have been reported in the literature. Section 3.3 shows the different doping strategies for Sb_2Se_3-based absorbers. Finally, the paper summarizes the challenges and outlines future perspectives for the development of Sb_2Se_3 photovoltaics, with a special emphasis on increasing conversion efficiency.

The authors believe that comparing and discussing the recently published works, with a special focus on ribbon orientation, ETL/HTL, and doping issues, can support future research to limit interface and defect recombination, especially affecting the open-circuit voltage (V_{oc}), and improve photocarrier extraction in Sb_2Se_3 solar cells.

2. Physical Vapor Deposition Techniques for Planar-Type Structure Sb_2Se_3 Solar Cells

Planar-configuration Sb_2Se_3 solar cells have generally achieved better performance than mesoporous structure cells, especially due to a higher open circuit voltage, V_{oc}. This is because in planar cells, defects introduced by chemical solvents, such as pinholes, are avoided, thus achieving a higher crystallinity.

Planar-type structures can be classified into two configurations: substrate and superstrate.

In the substrate architecture, the device configuration generally includes (starting from the top):

- A transparent electrode layer or metal grid (Al or Au)
- A window layer (for example undoped ZnO)
- An ETL (for example CdS)
- An Sb_2Se_3 absorber layer
- An HTL
- A metallic or conductive oxide back-contact
- A glass substrate.

The substrate architecture comes from the CIGS technology, which exhibits main advantages, such as the versatility in choosing different substrates and the possibility of fabricating tandem, bifacial, and eventually flexible cells [10].

Superstrate solar cells are a type of solar cell where the absorber layer is deposited on top of the other layers. This is in contrast to a substrate solar cell, where the absorber layer is deposited on the bottom.

In superstrate solar cells, the device configuration is generally formed by [10]:

- A metal contact
- An HTL (for example Spiro-MeOTAD, P3HT, NiOx)
- An Sb_2Se_3 absorber layer
- An ETL (for example TiO_2 or CdS)
- A transparent conductive oxide
- Glass (substrate).

Superstrate configuration cells take origin from the CdTe technology and generally exhibit the highest PCE values. This is because the interfaces in superstrate cells are less prone to defects.

In this section, we briefly describe the most interesting PDT for the growth of Sb_2Se_3 absorber layers:

- Magnetron sputtering;
- Close-spaced sublimation (CSS);
- Rapid thermal evaporation (RTE);
- Vapor transport deposition (VTD);
- Injected vapor deposition (IVT);
- Pulsed laser deposition (PLD);
- Pulsed electron deposition (PED).

2.1. Magnetron Sputtering

In radiofrequency magnetron sputtering (RF-MS), argon ions are accelerated by a radiofrequency electric field to hit a target. This removes material from the target, which is then deposited on a substrate that can be heated (Figure 2a).

Sb_2Se_3 is obtained by sputtering material from a high-purity, stoichiometric Sb_2Se_3 target at a working pressure of 0.5–1.5 Pa [17–19]. The chamber is filled with pure argon gas (99.99%). The RF power is fixed at 30–40 W.

In an alternative method proposed by C. Ma et al. [20], Sb_2Se_3 films can be deposited through co-sputtering of Sb_2Se_3 and Se targets. The pressure is maintained at 0.5 Pa. The RF power on the Sb_2Se_3 target is fixed at 30 W, while the RF power on the Se target is changed during the processing from 0 W to 15 W.

In another method, a thin film of metallic Sb is deposited by RF magnetron sputtering from a high-purity and dense Sb sputtering target. Highly crystalline Sb_2Se_3 thin films are obtained by a post-growth post-selenization heat treatment to induce the in situ combination reaction (from Se highly pure powder) [21].

2.2. Close-Spaced Sublimation

In CSS, the source material and the substrate are close to each other, at 1–5 mm, at the extremities of a graphite box. Deposition occurs in a vacuum atmosphere (or in certain cases in gases such as H_2, argon, nitrogen). The solid-state source (powder) and the substrate are heated at different temperatures: the former is heated to a temperature that favors sublimation (Figure 2b) while the latter is kept at a lower temperature to promote the condensation in thin-film form. The method offers the advantage of high deposition rates, and it is widely used to deposit semiconductor materials such as CdTe [22]. More recently, this method was also used to fabricate Sb_2Se_3–based solar cells [23,24]. Thanks to the low melting point of Sb_2Se_3 (608 °C) and the high saturated vapor pressure (around 100 Pa at 550 °C), CSS is a low-energy-consumption technique for Sb_2Se_3 growth, and it is more likely to form (hkℓ)-oriented grains with $\ell \neq 0$, especially at certain substrate temperatures. An optimal ribbon orientation allowed the CSS-grown Sb_2Se_3 solar cell to reach a high 9.2% efficiency [25].

2.3. Rapid Thermal Evaporation

RTE [6,26,27] is a vacuum process similar to CSS, but in this case, the material melts and evaporates from the liquid phase, not from the solid phase as in a sublimation process.

The deposition method is carried out in a tube furnace, generally maintained at a low vacuum by a mechanical pump (0.5–1 Pa) [6,25]. The distance between source and substrate is within 10 mm. In this process, a rapid increase in temperature and fast deposition are possible, so growth times are generally limited to a few seconds.

For example, H. Guo et al. [26] set a deposition time of 40 s, a preheating temperature of 310 °C for 20 min and the deposition temperature of 570 °C. A PCE of 7% was obtained for a simple Au/Sb_2Se_3/CdS/ITO/glass superstrate solar cell.

2.4. Vapor Transport Deposition

In the VTD method, both the substrate temperature and source-to-substrate distance can be adjusted. A carrier gas is saturated with a vapor from a subliming source (high-purity powder) and conducted towards the substrate at lower temperature, where the film growth occurs (Figure 2c). Sb_2Se_3 absorber-based solar cells fabricated through VTD exhibited an efficiency of 7.6% in a Au/Sb_2Se_3/CdS/ITO/glass solar cell structure [28].

2.5. Injected Vapor Deposition

IVD has been recently developed by Z. Duan et al. [29]. It is a promising technique for the fabrication of Sb_2Se_3 solar cells because it has been demonstrated to achieve one of the highest efficiencies (more than 10%) measured so far.

In an IVD system, the precursor of the Sb_2Se_3 powder is placed into a roller, which is heated at 490 °C. Argon gas is injected from one side of the roller and forms an Sb_2Se_3 vapor which reaches the heated substrate on the opposite side (Figure 2d). In IVD, the injection gas flow is the most crucial parameter affecting the quality of the material and thus the solar cell performance.

2.6. Pulsed Laser Deposition

In PLD, usually in a vacuum chamber, the plume is formed by a high-power pulsed laser beam that hits a target of the material that must be deposited (Figure 2e). The deposition occurs when the material condensates on the substrate, facing the target, which is maintained at an adjustable temperature. An Sb_2Se_3 absorber deposited at 500 °C by PLD reached an efficiency of 4.77% [30,31].

2.7. Pulsed Electron Deposition

PED is a physical deposition technique where a pulsed electron beam is accelerated by a high voltage to ablate a solid material target. The interaction between electrons and target material forms a plasma plume through the fast sublimation of the target which condensates on the surface of a substrate, placed at a few centimeters in front of it (Figure 2f). The nonequilibrium fast solid-vapor transition induces a transfer of material with the same stoichiometry as the target to the substrate. Sb_2Se_3 layers have been grown in an argon atmosphere of 0.3 Pa, setting a discharge voltage of 16 kV, a pulse rate of 9 Hz, with the substrate temperature maintained between 200 and 400 °C. The optimized solar cell based on an Sb_2Se_3 absorber grown by PED (with the substrate structure AZO/ZnO/CdS/Sb_2Se_3/Mo/glass) showed an efficiency of 2.1% [32,33].

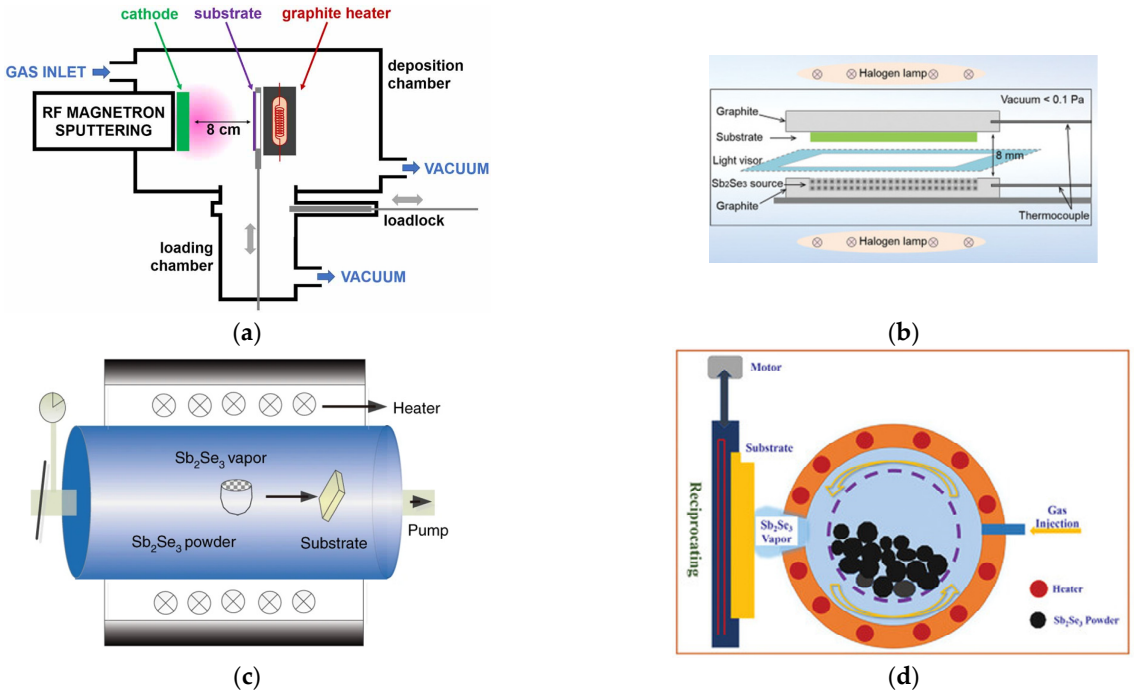

Figure 2. *Cont.*

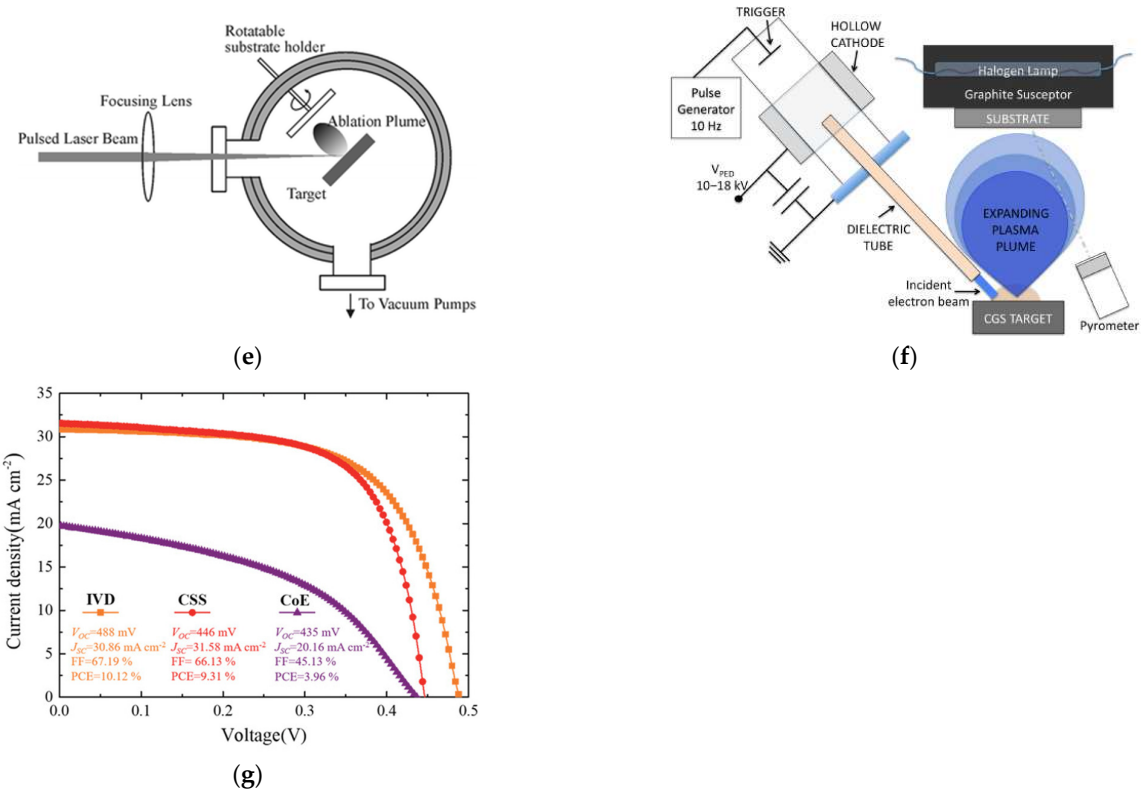

Figure 2. Schematized setups of different PVD systems: (**a**) RF-MS. Reproduced with permission from [19]. © 2021 IOP Publishing. (**b**) CSS. Reproduced from [34]. © 2020 K. Shen et al. Published by WILEY-VCH Verlag GmbH & Co. KGaA, Weinheim. (**c**) VTD. Reproduced from [28]. © 2018, X. Wen et al., http://creativecommons.org/licenses/by/4.0/ (accessed on 15 September 2023). (**d**) IVD. Reproduced with permission from [29]. © 2022 John Wiley & Sons. (**e**) PLD. Reproduced with permission from [31]. © The Royal Society of Chemistry 2004. (**f**) PED. Reproduced with permission from [33]. © 2013 IOP Publishing. (**g**) Current density–voltage (J–V) curves of the IVD-, CSS-, and CoE (co-evaporated)-Sb_2Se_3 solar cells. Reproduced with permission from [29]. © 2022 John Wiley & Sons.

3. The Main Challenges for Sb_2Se_3—Based Solar Cells (1D-Ribbon Alignment, HTL/ETL, Interfacial Engineering and Band Alignment, Doping)

3.1. One-Dimensional-Ribbon Alignment

As discussed in Section 1, Sb_2Se_3 is characterized by a one-dimensional crystal structure, a ribbonlike morphology, which determines strong anisotropic electrical conduction and optical properties (Figure 3). Crystal orientation control is crucial for the deposition of high-quality Sb_2Se_3 films. Sb_2Se_3 has a one-dimensional crystal structure, which gives it strong anisotropic electrical conduction and optical properties. Researchers are working hard to obtain vertically (or quasi-vertically) oriented Sb_2Se_3 ribbons, i.e., parallel to the growth direction. Several factors influence the crystal orientation of Sb_2Se_3, including the deposition technique, the substrate, the postdeposition treatments, and the use of pre-growth seeding methods. It is known that the best transport properties for PV applications can be achieved if the *c* axis of the crystal structure is normal to the surface (0,0,ℓ), while the worst conditions are obtained when the *c* axis lies on the surface (h,k,0). It is difficult to compare different results in the literature in terms of grain orientations and their correlation to photovoltaic performance. This is because the relative texture coefficient, TC (hkℓ), is rarely reported. TC (hkℓ) is the ratio between the measured (hkℓ) peak intensity and the intensity of the same peak for a reference, randomly oriented powder, weighted as a

percentage of the summation of the same value for all chosen peaks [35]. On the other hand, not all the reflections are always considered. TC (hkℓ) is given by the following equation:

$$TC(\mathrm{hk}\ell) = \frac{\frac{I(\mathrm{hk}\ell)}{I_0(\mathrm{hk}\ell)}}{\sum_n \frac{I(\mathrm{hk}\ell)}{I_0(\mathrm{hk}\ell)}} \times 100\ (\%)$$

where I_0 (hkℓ) is the relative intensity of the reflection with (hkℓ) Miller indices reported in the JCPDS card, and I(hkℓ) is the net intensity measured by the experimental XRD patterns after the background subtraction.

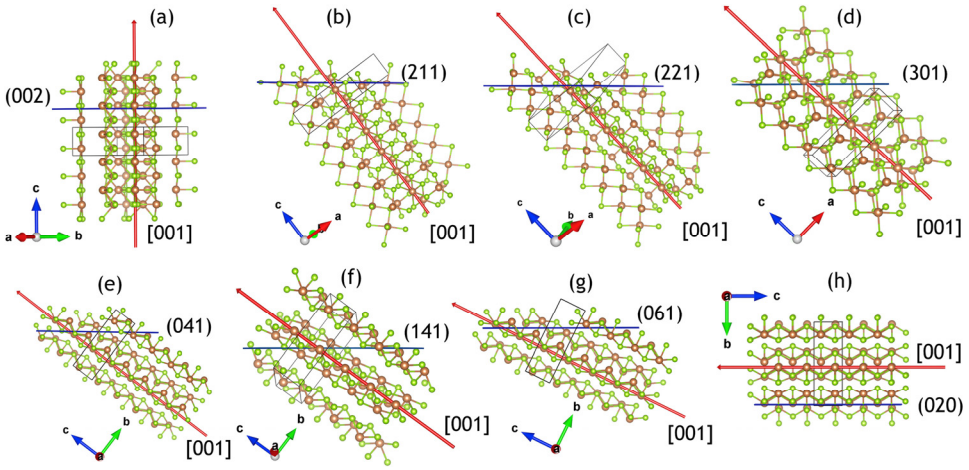

Figure 3. Graphical representations of the $(Sb_4Se_6)_n$ ribbons inclination (red arrow, Sb^{3+} = brown dots, Se^{2+} = green dots) corresponding to the (001) direction with respect to the growing surface (blue line) under different out-of-plane grain orientations (hkℓ): (**a**) (002), (**b**) (211), (**c**) (221), (**d**) (301), (**e**) (041), (**f**) (141), (**g**) (061) and (**h**) (020), respectively.. Reproduced with permission from [32], © 2020 Elsevier B.V.

In Table 1, we list several works where relative TC (hkℓ) (for the summation of reflections h = 0, k = 0, and $\ell \neq 0$) for Sb_2Se_3 films have been extrapolated from the reported graphs and at least around 10 reflections have been shown. The Σ TC ($\ell \neq 0$) parameter represents the percentage of vertically oriented ribbons. Vertically oriented ribbons do not lie on the substrate surface, and thus, they contribute to the electrical conduction.

Table 1. Extrapolated Σ TC ($\ell \neq 0$) values and reported PCE and J_{sc} for different deposition methods and underlying layers.

Deposition Method	Substrate/ Underlayer	Σ TC (hkℓ) $\ell \neq 0$	Observations	PCE	J_{sc} (mA/cm^2)	Reference
CSS	TiO_2/FTO/glass	86%	With seeding layer	3.8%	21.1	[36]
CSS	TiO_2/FTO/glass	65.4%	W/o seeding layer	1.6%	24.9	[36]
CSS	CdS/FTO/glass	89.5%	$CdCl_2$ treatment	6.23%	27.36	[36]
CSS	CdS/FTO/glass	88.1%	//	4.27%	21.74	[21]
CSS	CdS/FTO/glass	97.5%	CdS by CCS	2.82%	19.5	[37]
CSS	TiO_2/FTO/glass	~100%	Seeding layer	5.28%	24.6	[37]
CSS	TiO_2/CdS/FTO/glass	~100%	//	2.07%	15.6	[37]
CSS	SnO_2/FTO/glass	58.3%	$CdCl_2$ treatment	//	//	[38]
CSS	SnO_2/FTO/glass	5.4%	No treatments	//	//	[38]

Table 1. *Cont.*

Deposition Method	Substrate/ Underlayer	Σ TC (hkℓ) ℓ ≠ 0	Observations	PCE	J_{sc} (mA/cm^2)	Reference
CSS	FTO/glass	92.2%	330 °C	9%	29.8	[39]
VTD	SnO_2/ITO/glass	91.4%	//	2.7%	19.3	[40]
VTD	TiO_2/ITO/glass	30.9%	//	2%	23.6	[40]
VTD	SnO_2/TiO_2/ITO/glass	~100%	//	4.8%	25.6	[40]
VTD	CdS/TiO_2/ITO/glass	64.7%	CdS-VTD	4.91%	28.6	[41]
VTD	CdS/TiO_2/ITO/glass	50.1%	CdS-CBD	4.24%	28.3	[41]
RTE	CdS/FTO/glass	90.4%	w/o KOH treatment	4.8%	28.13	[26]
RTE	CdS/FTO/glass	92.1%	with KOH treatment	7.16%	//	[26]
RF sputtering	CdS/FTO/glass	71.3%	Annealing at 460 °C	6.06%	25.91	[42]
RF sputtering	FTO/glass	60%	//	1.28%	24.83	[19]
RF sputtering	CdS/FTO/glass	91%	//	2.36%	27.06	[19]
RF sputtering	Mo	30%	//	0.24%	5.11	[19]
PED	FTO/glass	60.2%	//	2.1%	20.3	[32]
PED	CdS/FTO/glass	38.4%	//	//	//	[32]
PED	Mo	0.6%	//	//	0.3	[32]
Thermal co-evaporation	Mo	73.5%	Substrate T = 300 °C	2.67–4.51%	19.51	[43]

In general, the CSS technique and the more recent IVD allow for more vertically oriented ribbons because the material is directly sublimated from the solid, and deposition occurs at high growth rates. In the paper by Krautmann et al., Sb_2Se_3 is deposited on TiO_2 with a seeding layer procedure: a 60 nm seed layer (SL) at 300 °C and then 1.8 micron at 450 °C [36]; the SL growth at low temperature is fundamental to create ribbonlike seeds on which subsequent columnar structures can grow. Vertical ribbons (002) planes show a TC of 1.2 for Sb_2Se_3 with an SL and 0.2 without an SL. The extrapolated Σ TC (hkℓ) $\ell \neq 0$ was 86% with an SL and 65.4% without an SL, respectively. As a consequence, solar cells with a higher TC show an efficiency of 3.8% and solar cells without an SL an efficiency of 1.6%, and an increase in the short circuit current density, J_{sc}, from 21.1 to 24.9 mA/cm^2 when the SL is used. In [44], the authors showed that the first grown 750 nm Sb_2Se_3 layer on CdS/FTO was compact, and ribbonlike structures started to grow at a higher growth time on the compact layer; (211), (221), (301), and (311) orientations prevailed when the entire film thickness was between 1.3 and 2.7 µm. A maximum PCE of 6.23% and a J_{sc} of 28.53 mA/cm^2 was obtained for a 2.1 µm thick Sb_2Se_3 with a Σ TC (hkℓ) $\ell \neq 0$ of 89.5%. The use of $CuInSe_2$ sensitizer quantum dots (QDs) to passivate defects of the Sb_2Se_3 nanorod structure allowed a 7.6% PCE.

In [34], the Sb_2Se_3 SL deposited by a CSS process on CdS was 10 nm thick and subsequently an Sb_2Se_3 absorber layer of 500 nm was deposited on the SL. In that case, the SL was grown by setting the source and substrate temperatures at 310 °C for 120 s, raising the source to 510 °C in 60 s (setting the substrate temperature at around 330 °C) and then keeping the source temperature at 510 °C for 10 s. The main absorber layer deposition was performed after a natural cooling to 270° of the substrate. In that case, the film grown after the seed layer showed a more (221) preferred orientation (Figure 4a), a PCE of 7.45%, and a J_{sc} of almost 30 mA/cm^2 was achieved for Au/t-Se/Sb_2Se_3/CdS/FTO cells.

L. Guo et al. [23] emphasized the importance of growth temperature and time during CSS growth. In fact, they observed that (211) oriented grains dominated in films thicker than 0.6 mm, and (hk0) orientations were strongly limited at substrate temperatures lower than 300 °C. Σ TC (hkℓ) $\ell \neq 0$ was 88.1% and graphite/Sb_2Se_3/CdS/FTO/glass samples reached a J_{sc} of 21.74 mA/cm^2 and a 4.27% PCE, in that case.

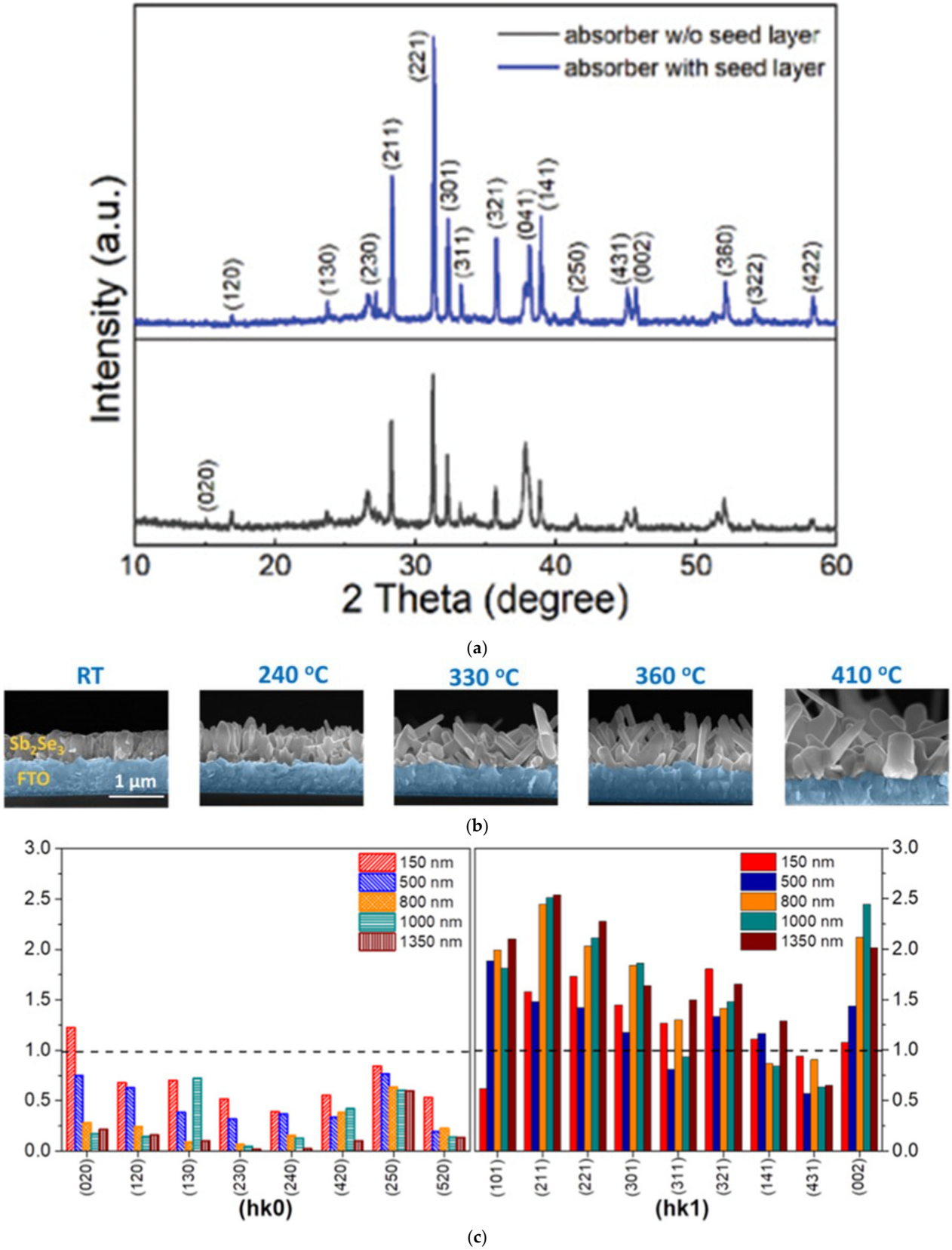

Figure 4. (**a**) XRD spectra of the Sb_2Se_3 films deposited by a seed layer-assisted successive CSS process and single CSS process. Reproduced from [34]. © 2020 K. Shen et al. Published by WILEY-VCH Verlag GmbH & Co. KgaA, Weinheim. (**b**) Cross-section images of Sb_2Se_3 absorber at different temperatures. (**c**) TC of Sb_2Se_3 absorber with different thicknesses. Reproduced with permission from [39]. © 2022 John Wiley & Sons.

Z. Li et al. [25] studied the evolution from a thin-layer film to a nanorod array for Sb_2Se_3 on Mo coated glass substrates deposited by CSS (Figure 5). As in the previous case, deposition time is important for 1D growth: they observed that the Sb_2Se_3 structure varied from a compact thin film to an aligned nanorod array with increasing growth durations (from 60 to 180 s). The nanorod alignment promoted a J_{sc} of 32.58 mA/cm^2 leading to a PCE of 9.2%.

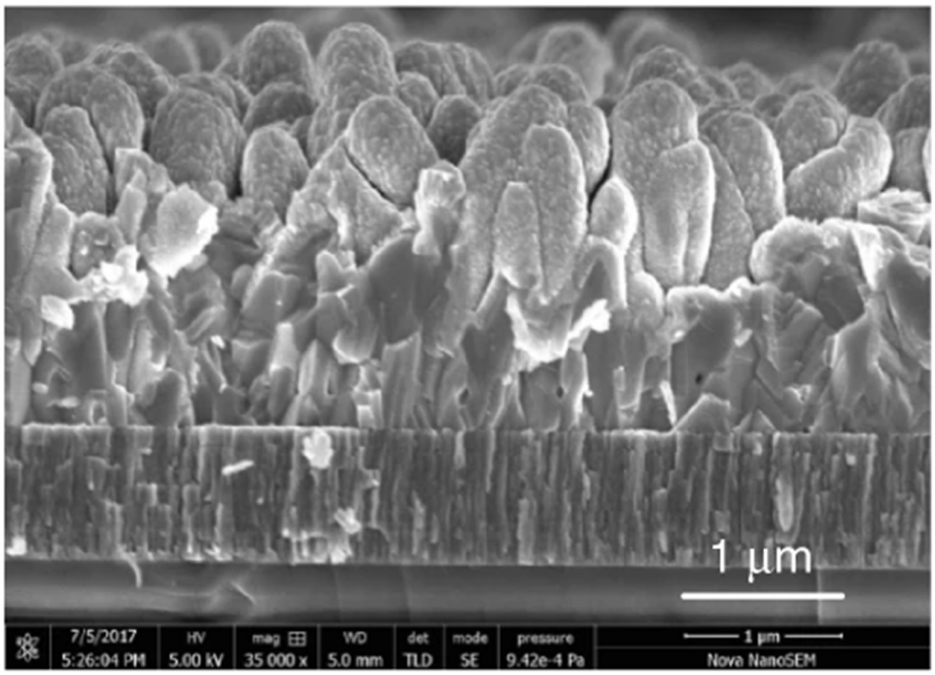

(**a**)

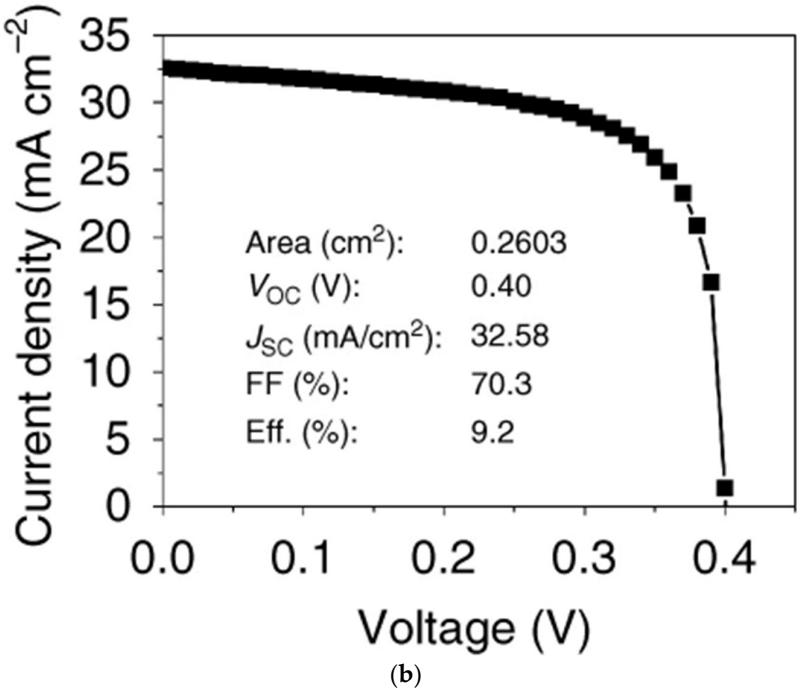

(**b**)

Figure 5. (**a**) Cross-sectional SEM image of the completed CdS/Sb_2Se_3 solar cells; (**b**) illuminated J–V curve of the same cell. Reproduced from [25]. Copyright 2019 Z. Li et al., http://creativecommons.org/licenses/by/4.0/ (accessed on 15 September 2023).

C. Guo et al. [45] studied the incorporation of a Ag element into Sb_2Se_3 obtaining quasi-vertical 1D ribbons at 280 °C, which vanished at 420 °C, where the (120) preferential orientation prevailed. Solar cells of AZO/ZnO/$(Sb_2Se_3)_x(AgSbSe_2)_{1-x}$/$MoSe_2$/Mo/glass achieved a J_{sc} of 25.29 mA/cm^2 and a 7.8% of PCE when the substrate temperature was set at 320 °C.

In [39], another CSS growth was adopted to obtain Sb_2Se_3, and the authors found that the formation of the Sb_2Se_3 crystal was not strongly dependent on the substrate temperature. However, (hk0) planes, parallel to the substrate, decreased for growth temperature >240 °C (up to 410 °C), while most of the TCs for the (hk1) planes, oblique or perpendicular to the substrate, increased with the growth temperature between 240 °C and 410 °C. Σ TC(hkℓ) $\ell \neq 0$ was 92.2% in this case and AZO/i-ZnO/CdS/Sb_2Se_3/FTO/glass solar cells with a 1350 nm (Figure 4b,c) thick Sb_2Se_3 layer demonstrated a J_{sc} of 29.5 mA/cm^2 and a conversion efficiency of 9.0%.

P. Fan et al. [46] investigated Sb_2Se_3 obtained by CSS followed by a selenization process on a Mo/SLG (soda–lime glass) substrate. They studied different temperature ramp for the source during sublimation: from 260 or 290 °C for 2 min to 510 or 520 °C for 2 min. In the selenization process, the Se powder and the as-grown Sb_2Se_3 thin film, placed at a distance of 23 cm, were simultaneously heated at 400 and 420 °C for 15 min, respectively. It was found that the (hk0) grain orientation decreased by increasing the temperature from 260 to 290 °C, while the TC values of the (hk1) and (hk2) increased with the temperature, finding an optimum substrate temperature to stimulate the (hk1) orientation for 290 °C. Moreover, the subsequent post-selenization treatment led to large grain sizes with the preferred (hk1) orientation. In these optimized conditions, the authors obtained a high 509 meV V_{oc}, with a J_{sc} of 21.15 mA/cm^2 reaching a PCE of 4.86% with a Ag/ITO/CdS/Sb_2Se_3/Mo solar cell.

N. Spalatu et al. [37] grew Sb_2Se_3 absorbers by CSS, finding a preferred orientation of grains along the (211) and (221) crystal directions for depositions at 450 °C. For temperatures rising from 300 to 450 °C, the TC values of the (301) and (151) planes increased systematically, and the TC of the (020) and (120) planes decreased. A maximum efficiency of 2.8% was demonstrated for Au/Sb_2Se_3/CdS/FTO/glass solar cells with an Sb_2Se_3 absorber obtained at 450 °C, with a Σ TC (hkℓ) $\ell \neq 0$ of 97.5%. Better performance of PCE around 5.3% was achieved with a superstrate configuration TiO_2/Sb_2Se_3 cell where an Sb_2Se_3 seed layer was implemented at the interface and where Σ TC (hkℓ) $\ell \neq 0$ was around 100%. The SL consisted of a ~60 nm thick Sb_2Se_3 layer deposited at a low T of 300 °C by CSS at the interface between buffer and absorber layers, and it was fundamental in that work to enhance the efficiency from 1.66% (J_{sc} of 19.8 mA/cm^2) to 5.28% (J_{sc} of 24.6 mA/cm^2).

A. Amin et al. [47] fabricated Sb_2Se_3 by CSS on a nanorods (NR)-CdS/nanoparticles (NP)-CdS buffer layer. The nanorod CdS (NR-CdS) buffer layer was synthesized by a hydrothermal method while the NP CdS films were prepared by the CBD method. The authors observed that the NR-CdS and NR-CdS/NP-CdS buffer layers favored the (211) orientation of the Sb_2Se_3 ribbons and the reduction in the (120) orientation. Thanks to the control of the nanoribbon orientation, the Sb_2Se_3 solar cell reached a PCE of 7.16%.

S. Pasini et al. [48] showed the Influence of the window layer on the Sb_2Se_3 ribbon orientation for a superstrate configuration solar cell. A preferential growth of the CSS-grown Sb_2Se_3 along the (001) direction on window layers containing zinc, with a TC for the (002) reflection reaching the maximum value of 27% and a 4.5% efficiency with a ZnCdS ($Zn_{0.15}Cd_{0.85}S$) window layer (with a solar cell structure of Pt/Sb_2Te_2/Sb_2Se_3/ZnCdS/ZnO/ITO/glass) was observed.

In the case of the VTD process, X. Wen et al. [28] obtained Sb_2Se_3 grown on CdS/ITO, studying an evaporation temperature between 480 and 510 °C, reached with a ramp rate of 20 °C/min followed by a plateau of 2 min. When the source temperature was at 510 °C, corresponding to a substrate temperature of 390 °C, the film exhibited the highest crystallinity and XRD intensity of the preferred (221) orientation. Thus, the Au/Sb_2Se_3/CdS/ITO/glass solar cells showed a J_{sc} of 29.9 mA/cm^2 leading to a 7.6% PCE.

J. Kim et al. studied Sb_2Se_3 deposition by VTD [49], by co-evaporation from Sb_2Se_3 and Se sources. The chamber pressure was 3 mTorr, with a source temperature of 560 °C and a substrate temperature of 300 °C. The authors observed that Se flux control was very important for the film characteristics. In fact, an extra supply of Se contributed to suppress undesirable vacancies V_{Se}, while an excessive Se overpressure inhibited the (221) orientation growth, which was detrimental to electrical transport properties. A superstrate configured solar cell ($Au/Sb_2Se_3/CdS/ITO/glass$) showed a PCE of 5.2% in optimized conditions. S. Dong et al. [50] proposed a modified VTD method, in a double-temperature-zone furnace, to obtain Sb_2Se_3 with Se in excess. A CdS/ITO/glass substrate was placed on the graphite bracket at the extremity of the furnace, the Se powder was kept at a higher temperature than the melting point (>270 °C) to ensure a stable supply of Se was placed at the other end of the tubular furnace above its thermal baffle, and two quartz crucibles containing Sb_2Se_3 powder were put in the center of the two temperature zones. The authors showed that (221) orientations increased with the Se flux; thus, with the Se excess, and a $Au/Sb_2Se_3/CdS/ITO/glass$ structure, the PCE was improved from 5.1% to 6.7%, and J_{sc} from 27.7 to 30.5 mA/cm^2 with the absorber grown in Se-rich conditions.

W. Wang et al. [40] implemented VTD-grown Sb_2Se_3 on SnO_2, TiO_2, SnO_2/TiO_2, CdS, and $SnO_2/TiO_2/CdS$ ETL. They observed that SnO_2 or/and SnO_2/TiO_2 ETL underlayers favored the formation of (041), (141), and (061) (Σ TC (hkℓ) $\ell \neq 0$ of 91.4% and almost 100%, respectively) more than in the case of TiO_2 (Σ TC (hkℓ) $\ell \neq 0$ of 30.9%). Since the CdS interlayer was also important to reduce the band offset, the $Sb_2Se_3/CdS/TiO_2/SnO_2/ITO/glass$ solar cell achieved a J_{sc} of 29.9 mA/cm^2 and PCE of 7%.

In [41], the authors fabricated a CdS layer by VTD with a better conductivity and higher crystallinity than with CBD. They observed that the CdS-buffer layer induced the growth of Sb_2Se_3 with an (hk1) orientation, such that the extrapolated Σ TC ($\ell \neq 0$) was around 64.7% for Sb_2Se_3 grown on a CdS layer deposited by VTD and 50.1% for the one grown on CdS obtained by CBD. Thus, they obtained a 4.91% PCE for the CdS-VTD-based device, and 4.24% for the CdS-CBD.

In [51], a CdS ETL was also modified with Al_2O3 grown by atomic layer deposition as the interface layer at the CdS/Sb_2Se_3 interface. The Sb_2Se_3 absorber layer was deposited on Al_2O3 by VTD in a dual-temperature-zone tube furnace, showing a strong increase in TCs of (hk1) and decrease in (hk0) in the presence of Al_2O_3. Therefore, the authors obtained a PCE of 6.25% for a carbon$/Sb_2Se_3/Al_2O_3/CdS/FTO/glass$ solar cell configuration.

V. Kumar et al. [52] compared thermally evaporated Sb_2Se_3 subjected to three different processes: just annealing, simultaneous evaporation of Sb_2Se_3/Se during the absorber growth, and post-deposition selenization. They observed that the Sb_2Se_3 layer grew spontaneously with predominant (221) and (321) orientations. Then, post-deposition annealing and co-selenization reduced (321) in favor of the (141) orientation, while in the case of the postselenization, the (221) orientation had a stronger intensity, and the (041) orientation was also present.

Surface treatments can also induce columnar-mode growth as observed from H. Guo et al. [53]. In that case, the RTE method was used to fabricate Sb_2Se_3 in a $Au/Al_2O_3/P^+$-Sb_2Se_3/P- $Sb_2Se_3/CdS/FTO/glass$ structure in which the CdS layer was submitted to an oxygen plasma treatment before the Sb_2Se_3 growth. The effect was a decrease in the CdS grain size, a reduction in film roughness, and the introduction of oxygen atoms. The authors argued that the increase in the O content in the CdS surface stimulated a higher crystallinity and the columnar growth of Sb_2Se_3, thus an increase in J_{sc} from 22.03 mA/cm^2 to 26.26 mA/cm^2 and PCE from 2.48 to 5.1% was observed for solar cells without or with plasma treatment, respectively. Moreover, a subsequent Al_2O_3 layer, deposited by atomic layer deposition (ALD) method, increased by two orders of magnitude the hole concentration for Sb_2Se_3 film, leading to a PCE of 6.7%.

In [54], an Sb_2Se_3 nanorod-array was prepared on the Mo substrate at a low temperature by RTE. The authors showed the importance of the SL growth temperature; the SL was performed at 360 °C while 480 °C was the Sb_2Se_3 growth temperature, resulting in a

preferred orientation in the (211) direction and a minimum TC value for the (230) diffraction peak. In this manner, they showed an efficiency of 6.3% in a ZnO/CdS/Sb_2Se_3/Mo/SLG solar cell structure.

X. Wen et al. [55] fabricated a highly (001)-oriented Sb_2Se_3 film on a flexible mica where Sb was thermally evaporated, followed by a selenization process into a horizontal quartz tube furnace at 410 °C. In this way, Ag/ITO/CdS/Sb_2Se_3/Mo/mica grid flexible solar cells obtained an efficiency of 8.42%, a J_{sc} of 31.30 mA/cm2, and a V_{oc} of 0.47 V.

A KOH treatment also induces preferential grain orientation, as observed in [26], where the TC ratio between the (221) and (211) peaks was higher in the Sb_2Se_3 film exposed to 0.07 M KOH than that in the not-treated films, showing a Σ TC (hkℓ) $\ell \neq 0$ higher than 90%. This concentration was found to be optimal, leading to a 7.16% efficiency and a J_{sc} of 30.68 mA/cm^2 in a Au/Sb_2Se_3/CdS/FTO/glass solar cell. At the same time, the KOH solution (0.07 M) treatment played a doping role, through a diffusion of K species; in fact, the hole concentration of the Sb_2Se_3 film increased from 10^{13} cm^{-3} to 10^{15} cm^{-3}; for higher concentrations (0.15 M), the carrier density decreased, probably due to corrosion.

J. Zhou et al. showed how the SnO_2 underlayer deposition and treatment could influence the Sb_2Se_3 orientation [38]. In that case, Sb_2Se_3 grown by CSS on treated SnO_2, with a $CdCl_2$ methanol solution, showed a high preferential (211) 1D orientation, Σ TC (hkℓ) $\ell \neq 0$ was 58.3% versus 5.4% for the not-treated surface. The authors claimed that this effect was due to the formation of Cd-$[Sb_4S_6]_n$ ribbon covalent bonds.

Now, considering the sputtering method, G-X. Liang et al. [17] obtained Sb_2Se_3 nanorods with the preferred crystallographic orientation of (221) at a substrate temperature of 375 °C, and a deposition pressure and power of 0.5 Pa and 30 W, respectively. The same conditions at room temperature led to amorphous Sb_2Se_3 films. AZO/ZnO/CdS/Sb_2Se_3 nanorods/Mo solar cells exhibited a 2.1% PCE.

R. Tang et al. [42] reported on a sputtered Sb_2Se_3 cell obtained by a two-step process (growth of amorphous Sb_2Se_3 by RF-MS followed by a selenization process). The selenization step was performed in an evacuated tubular furnace successively filled with pure Ar at a pressure of 5×10^4 Pa. The highly pure Se powder was heated at 400 °C while Sb_2Se_3 was kept at a lower temperature. Temperature is critical during selenization so that the growth of vertical rods is favored when selenization is performed up to 420 °C, then (hk0)-oriented grains start to increase. For the best T, Σ TC (hkℓ) $\ell \neq 0$ was 71.3%, J_{sc} was 25.91 mA/cm^2, and the efficiency of a Ag/ITO/CdS/Sb_2Se_3/Mo reached 6.06%. For S. Rijal et al. [56], in Sb_2Se_3 grown by CSS on Mo-coated glass, higher temperatures in selenization enhanced crystallinity, as the average grain size increased with the selenization temperature. The highest TC values of the (211) and (221) planes for the film annealed at 425 °C indicated a preferred Sb_2Se_3 ribbon orientation at this selenization temperature. As a consequence, J_{sc} increased from 18.6 mA/cm^2 to 22.9 mA/cm^2, and the PCE from 1.85% to 6.43%.

C. Yuan et al. obtained [57] an Sb_2Se_3 film by a two-step method: DC-MS of metallic Sb followed by selenization through a rapid thermal process (RTE). The selenization process was conducted with temperatures between 320 and 440 °C for 5 min, under vacuum conditions. The thin films selenized with temperatures below 400 °C exhibited a preferred orientation along the (211) plane and (221) plane, while the morphology quality decreased for higher annealing temperatures with the appearance of holes and a lower carrier mobility. The best achieved efficiency for an Al/Al:ZnO/ZnO/CdS/Sb_2Se_3/Mo solar cell was 3.47%, and J_{sc} = 16 mA/cm^2 for selenization performed at 400 °C.

G. Spaggiari et al. [19] observed that the crystal structure and the $(Sb_4Se_6)_n$ ribbon orientation of Sb_2Se_3 obtained by RF sputtering were strongly dependent on the deposition temperature and type of substrate. The authors tested different types of substrate/underlayers (glass, Mo, FTO, CdS, and ZnO) observing a thermodynamical grain alignment along the (001) direction, vertical with respect to the substrate, for depositions at 300 °C on thick samples grown on CdS (Σ TC (hkℓ) ($\ell \neq 0$) = 91%) and ZnO (Σ TC (hkℓ) ($\ell \neq 0$) = 80%). An efficiency of 2.36% was reached, with a J_{sc} of 27.06 mA/cm^2 for a

$Au/Sb_2Se_3/CdS/FTO/glass$ superstrate configuration solar cell while the PCE was very poor for the absorber grown on Mo substrates.

I. Caño et al. [58] obtained Sb_2Se_3 layers on Mo-sputtered SLG substrates by a selenization of thermally evaporated Sb. The (002) (vertical ribbons) reflection was predominant for Se-rich conditions, while in Sb-rich conditions, the (231), (141), and (221) peaks became dominant. In detail, with 0.36 Se, a slightly poor Se compound, (002) reflections practically disappeared, while Se-rich conditions could also reduce the V_{Se}-type defects and thus improve the device performance.

Y. Yang et al. [59] fabricated a $Au/Sb_2Se_3/CdSe/FTO/glass$ solar cell by obtaining CdSe and Sb_2Se_3 both by PLD, with the $CdSe/Sb_2Se_3$ bilayer deposited continuously in the same chamber. The authors studied the CdSe temperature influence on Sb_2Se_3 quality, maintaining a deposition temperature of Sb_2Se_3 at 500 °C and varying the CdSe temperature: when it is increased to 300 °C, the TCs of the (221) and (221) orientations increased, while the (120)- and (230)-orientation TCs decreased, showing a 1D preferential growth for these conditions. $Au/Sb_2Se_3/CdSe/FTO/glass$ solar cells exhibited a J_{sc} of 20.18 mA/cm^2 and a PCE of 3.65% for a CdSe deposition temperature of 300 °C.

PLD growth of Sb_2Se_3 films deposited on $CdS/FTO/glass$ was performed by K. Yang et al. [30] at a substrate temperature of 500 °C, a repetition rate of 6 Hz, and a pulse energy of 90 mJ. The samples showed a preferred direction of (221) and a J_{sc} of 31.68 mA/cm^2, and an efficiency of 4.77% was achieved.

In the only paper (to date) reporting on PED deposition, the role of the substrate was crucial for the 1D ribbon vertical alignment; in fact, F. Pattini et al. [32] showed that the best ribbon alignment for Sb_2Se_3 grown on FTO/glass (Σ TC (hkℓ) ($\ell \neq 0$) = 60.2%), while for CdS, this value decreased to 38.4% and, differently, ribbons were completely laid on the substrate surface when Sb_2Se_3 was grown on Mo (Σ TC (hkℓ) ($\ell = 0$) = 99.4%). As a consequence, a very low J_{sc} was obtained for Sb_2Se_3 deposited on Mo, while $AZO/ZnO/CdS/Sb_2Se_3/FTO/glass$ solar cells exhibited a J_{sc} of 20.28 mA/cm^2 and a PCE of 2.1% under frontal illumination and an equivalent 3.1% conversion efficiency for a bifacial illumination.

S-N. Park et al. [43] applied a co-evaporation method with Sb_2Se_3 and Se sources to obtain an Sb_2Se_3 absorber for solar cells and observed that the fine control of process temperature was extremely crucial; in fact, (hk1)-oriented Sb_2Se_3 ribbons were favored when the substrate was heated in the range between 270 °C and 315 °C; in particular, rod arrays preferentially oriented along (hk1) were obtained for 315 °C, while 330 °C stimulated the growth of hk0 planes. In these conditions, an extrapolated Σ TC (hkℓ) $\ell \neq 0$ was 73.5%. The authors proposed a nucleation and growth model for explaining the influence of the substrate temperature on the thin film formation, in particular, the evolution of Sb_2Se_3 from flat to rods with the increasing substrate temperature, based on a Terrace–Ledge–Kink model. The (001), (211), and (221) surfaces presented higher surface energies than (100), (010), (110), and (120), which had no dangling bonds and tended to form terraces. On the other hand, (hk1) surfaces had large numbers of dangling bonds and presented many kink and ledge sites. Increasing temperatures and consequently the diffusion length stimulated the adatom to migrate to these sites. As the propagation direction was expected to be (001) because of the large number of dangling bonds, a growth of rods along the vertical direction was predicted. The rod array obtained at 315 °C implied a highest PCE of 4.5% and a J_{sc} of 25.39 mA/cm^2 for $Au/AZO/ZnO/CdS/Sb_2Se_3/Mo$ solar cells.

A summary of the reviewed deposition techniques, the TC values, different solar cell architectures, and the correlated performances obtained is reported in Table 1. In Figure 6, the extrapolated Σ TC (hkℓ) ($\ell \neq 0$) values are plotted as a function of PCE for different solar cells. Even though the points are slightly scattered, a clear trend between TC and PCE can be observed. Even if the PCE value also depends on other electrical parameters, on the different HTL and ETL materials, and even on the peculiar deposition method, one can argue that high-efficiency cells must have a high degree of vertical ribbon orientation.

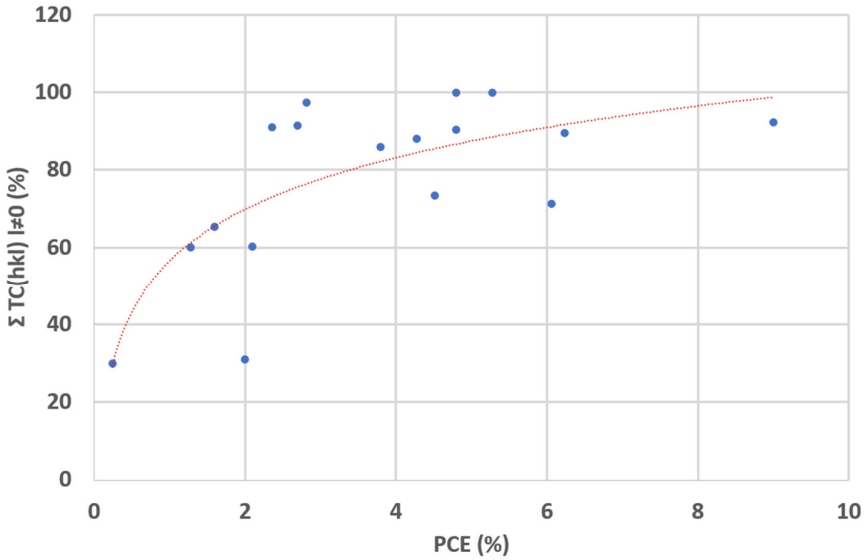

Figure 6. Extrapolated Σ TC (hkℓ) ($\ell \neq 0$) values versus PCE.

3.2. HTL/ETL, Interfacial Engineering, and Band Alignment

V_{oc} in Sb_2Se_3 solar cells is strongly affected by the interface and SRH recombination. In order to recover V_{oc} losses, the optimization of the band alignment is fundamental to suppress the interface and defect recombination. In semiconductors, offsets between conduction bands and valence bands at the interfaces of the heterostructures are fundamental for the good working of solar cells. A minimization of the band offset should be achieved, and a "spike-like" configuration is more adequate, where the offset is positive, hence the conduction band minimum of the absorber is lower than the conduction band minimum of the buffer/window layer [60]. The choice of ETLs and HTLs controls the energy band alignments in Sb_2Se_3 solar cells. Different ETLs and HTLs have been explored in the literature to find the optimal solar cell configuration.

3.2.1. ETLs

Among ETLs, CdS is largely used as it is commonly employed as a buffer layer in CIGS, CdTe, and CZTSSe solar cells and it is easily obtained by CBD. The conduction band offset (CBO) at the CdS/Sb_2Se_3 interface [61] is a type-II band alignment, the corresponding calculated CBO and valence band offset (VBO) at the CdS/Sb_2Se_3 interface are 0.24 and 0.94 eV, respectively (Figure 7). However, Cd-free ETLs are objects of study to avoid the toxicity of Cd and other drawbacks associated with CdS, such as a high lattice mismatch (>10%) with Sb_2Se_3, undesired absorption, the need for surface treatments, and the Cd interdiffusion at the Sb_2Se_3/CdS interface which causes further defects [62].

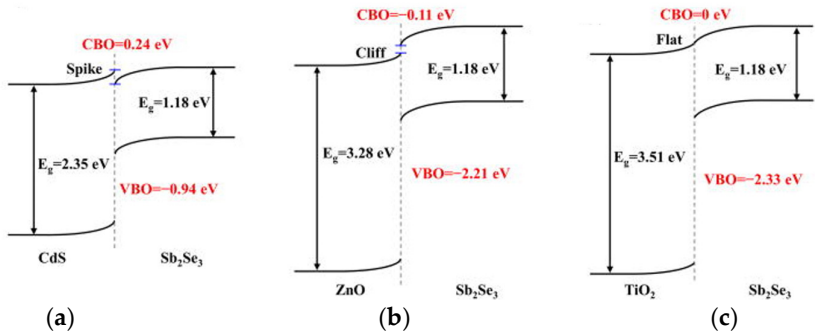

Figure 7. Band alignments between Sb_2Se_3 and different buffer layers—CdS (**a**), ZnO (**b**), and TiO_2 (**c**). Reproduced from [61], with the permission of AIP Publishing.

On the other hand, SnO_2, TiO_2, and ZnO, have similar lattice parameters with Sb_2Se_3. These kind of ETLs have been predominantly explored in superstrate configurations. The ZnO/Sb_2Se_3 interface presents a cliff-type CBO of 0.11e V and a VBO of 2.21 eV, while TiO_2/Sb_2Se_3 present a flat interface for CBO and a VBO of 2.33 eV [61]. S. Lu et al. conclude that a promising strategy would be to combine CdS and TiO_2 with Sb_2Se_3 in order to obtain a favorable spikelike band alignment.

Alternative ETLs, investigated in theoretical studies are WS_2 [63], CdZnS [64], CdS-3N, ZnMgO [65], and ZnSe [66].

CdS as an ETL has been investigated by several groups in Sb_2Se_3 solar cells. More recently, modified CdS layers were studied for interface engineering, to modify the CdS/Sb_2Se_3 heterojunction from a "cliff-like" structure to a "spike-like" structure. Y. Luo et al. [67] obtained an Al^{3+} cation doping in the CdS buffer layer (ETL) through spin-coating and postannealing methods. The Al doping allowed the optimization of the band alignment with an ideal CBO, modifying it from a "cliff-like" structure to a "spike-like" one, thus reducing the charge recombination. Sb_2Se_3 was obtained by Sb RF-MS deposition and subsequent selenization while the Al-doped CdS film was obtained via direct current (DC) MS. Solar cells with a $Ag/ITO/CdS:Al/Sb_2Se_3/Mo$ structure achieved a PCE of 8.41%, J_{sc} = 28.26 mA cm^{-2}, V_{oc} = 489 mV, and FF = 60.87%.

In another work, a CdS ETL was also treated by using nontoxic $SbCl_3$ to form an $Sb\text{-}CdS/Sb_2Se_3$ interface [68], which also produced a "spike"like-type heterojunction. A $Au/spiro\text{-}OMeTAD/Sb_2Se_3/CdS/FTO/glass$ superstrate structure delivered a PCE of 6.13%, while with a normal CdS/Sb_2Se_3 interface, the PCE was 3.95%. The authors observed that this $SbCl_3$ treatment induced the formation of pure hexagonal CdS which stimulated the growth of an Sb_2Se_3 film with a (hk1) preferential orientation.

J. Cheng et al. fabricated a Cd(S,O) ETL [69] through a sol–gel method; the oxygen content was controlled using an anhydrous spin solution. The possibility of changing the Cd/S content ratio permitted the optimization of the CdS layer properties. A $Au/Sb_2Se_3/CdS(O)/ITO$ solar cell structure reached an improved efficiency of 5.76% for a Cs:S ratio of 1:0.85.

An oxygenated CdS (CdS:O) ETL was investigated by Y. Liu et al. [70]. CdS:O was obtained by reactive sputtering with a CdS target and an Ar/O_2 mixed working gas, while the Sb_2Se_3-absorbed layer by CSS with a thickness between 1200 nm and 1500 nm. An $AZO/ZnO/CdS:O/CdS/Sb_2Se_3/MoSe_2/Mo/glass$ solar cell with an O_2 content of 0.5% in the sputtering environment achieved V_{oc} = 408 mV, J_{sc} = 28.11 mA cm^{-2}, FF = 66.98%, and PCE = 7.69%.

L. Guo et al. [71] also studied CdS:O obtained by RF sputtering as an ETL for Sb_2Se_3-based solar cells grown by CSS. Sputtered CdS:O exhibited a better quality than CdS deposited by CBD; the preferred grain orientation was (211) in $CdS:O/Sb_2Se_3$, while it was (221) in CBD CdS/Sb_2Se_3. Oxygen also played a role in blocking the interdiffusion of Cd into the Sb_2Se_3 film. Thus, the PCE was increased from 6.1 to 7% from a CBD CdS to a sputtered CdS:O in the $Ag/graphite/Sb_2Se_3/CdS:O/FTO/glass$ solar cell configuration.

X. Mao et al. [72] employed a CdS/SnO_2 ETL in a $Au/Spiro\text{-}OMeTAD/Sb_2(S,Se)_3/CdS/SnO_2/FTO/glass$ solar cell, achieving a PCE of 8%. In their work, they highlighted the importance of synthesis and specifically the ratio between SnO_2 hydrosol and deionized water during a spin-coating method on the performance of the cells.

G. Li et al. [73] studied a CdZnS ETL, for a $ZnO:Al/ZnO/Cd_xZn_{1-x}S/Sb_2Se_3/Mo/glass$ solar cell with a $Cd_{0.75}Zn_{0.25}S$ buffer layer. They obtained an efficiency of 6.71%, compared to the CdS/Sb_2Se_3-based cell that achieved a PCE of 5.08%. The optimum concentration allowed the formation of a spikelike interface with a CBO of 0.34 eV, which reduced the photocarrier recombination.

SnO_2 has been studied as a valid alternative to CdS thanks to the interesting band alignment with Sb_2Se_3 (spikelike heterojunction) and high electron mobility. J. Zhou et al. [74] studied SnO_2, obtained by a spin-coating method, treated with $CdCl_2$ as an ETL for Sb_2Se_3 cells. They observed that the $CdCl_2$ treatment was fundamental to grow

vertically oriented Sb_2Se_3 ribbons; in fact, efficiency improved strongly from 0.12 to 4.76% when SnO_2 was treated in a C/P3HT/Sb_2Se_3/SnO_2/FTO/glass solar cell.

W. Wang et al. [40] explored a double interface SnO_2/TiO_2/CdS ETL for VTD-grown Sb_2Se_3 in a superstrate configuration, obtaining a 7% PCE, as already mentioned.

S. Wen et al. [75] also showed the importance of the $CdCl_2$ treatment on a SnO_2 ETL in a Au/Sb_2Se_3/SnO_2/ITO/glass solar cell measuring efficiency increases from 2.02 to 4.03% when the treatment was performed.

Z. Chen et al. [76] studied La-doped SnO_2 as an ETL, obtaining an efficiency of 3.25% for Au/Sb_2Se_3/SnO_2/FTO/glass solar cells. The authors observed that La doping improved the crystallinity and electrical conductivity of SnO_2 films.

$CdCl_2$ treatment was also investigated by Y. Wang et al. [77], this time on TiO_2. The importance of this treatment was clear since the Sb_2Se_3 device's PCE improved from 2.02 to 6.06% with the Au/Spiro-OMeTAD/Sb_2Se_3/TiO2/FTO/glass device structure when $CdCl_2$ was used on TiO_2. As a consequence of the treatment, the CBO of the Sb_2Se_3/TiO_2 heterojunction reduced from 0.50 to 0.20 eV producing a narrower clifflike CBO of the Sb_2Se_3/TiO_2 heterojunction, which favored a passivated interface recombination and facilitated the electron transportation from Sb_2Se_3 to TiO_2.

X. Wang et al. [78] fabricated Au/Sb_2Se_3/CeO_2/CdS/FTO/glass solar cells, exploring ultrathin cerium dioxide (CeO_2) obtained by evaporation, together with CdS as ETLs. A CeO_2 layer of 2 nm stimulated the (221) orientation in Sb_2Se_3 ribbons and the solar cell exhibited a 5.14% PCE. The authors attributed the increase in PCE to an improvement in crystallinity and a reduction in photocarrier recombination at the interface between Sb_2Se_3 and CdS, due to the larger (3.2 eV) energy gap of CeO_2.

J. Zhang et al. [79] used an n-type MoO_3 layer as the ETL obtaining a 6.3% conversion efficiency in a Au/MoO_3/Sb_2Se_3/CdS/FTO/glass superstrate solar cells, optimizing MoO_3's thickness and substrate temperature during its deposition (Figure 8).

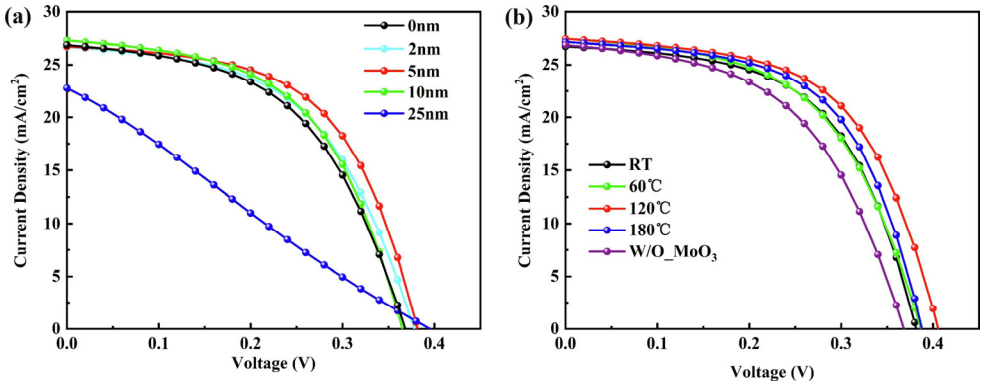

Figure 8. J–V curves of solar cells with (**a**) different thickness of MoO_3 layers, (**b**) different substrate temperatures during deposition of 5 nm MoO_3. Reproduced with permission from [79], ©2021 Elsevier B.V.

Alternative Cd-free solar cells have been a strategic goal in order to achieve an environmentally sustainable PV technology. W. Wang et al. obtained TiO_2/SnO_2 double ETLs, treated with $SbCl_3$, demonstrating a PCE of 5.82% in a Au/Sb_2Se_3/TiO_2/SnO_2/ITO/glass solar cell [80].

$Zn_{1-x}Sn_xO$ layers [81] were obtained via magnetron cosputtering as an ETL. The authors obtained a PCE of 3.44% for a Ag/ITO/ZTO/Sb_2Se_3/Mo/glass substrate solar cell, exploiting a $Zn_{0.57}Sn_{0.43}O$ buffer layer.

Y. Dong et al. [82] investigated a $ZnCl_2$-modified In_2S_3 ETL also for a Cd-free solar cell in a Au/Spiro-OMeTAD/Sb_2Se_3/In_2S_3/FTO solar cell. A $ZnCl_2$ post-treatment favored a quality improvement of the In_2S_3 film, prepared by CBD, also inducing a longitudinal growth on the Sb_2Se_3 layer, fabricated via VTE. Thus, on $InCl_2$–In_2S_3, $(Sb_4Se_6)_n$ ribbons

exhibited a perpendicular orientation to the substrate surface. The solar cell PCE increased from 2.63% to 5.00% due to the $ZnCl_2$ treatment.

ZnSe as an alternative ETL was studied theoretically by R. Kumari et al. with SCAPS-1D and the Al/ZnSe/Sb_2Se_3/Mo solar cell efficiency was 24% with optimized parameters [66].

Moreover, an organic ETL was recently studied for Cd-free Sb_2Se_3-based solar cells. For example, C60 was used in [83] for an Al/Alq3(3.0 nm)/C60 (5.0 nm)/Sb_2Se_3 (∼50 nm)/NPB (6.0 nm)/ITO/glass solar cell, in which a PCE of 5.03% was demonstrated. In that paper, the NPB (N,N′-Di(1-naphthyl)-N,N′-diphenyl-(1,1′-biphenyl)-4,4′-diamine) layer was successfully used to facilitate the Sb_2Se_3 crystallization, ribbon orientation, and photocarrier recombination suppression.

D. Rovira et al. [84] presented a polymeric ETL in a CdS-free solar cell, with an AZO/b-PEI/ZnO/Sb_2Se_3/Mo/glass structure. Sb_2Se_3 was obtained by the evaporation of 280nm-thick Sb film on the deposited Mo and a subsequent annealing in a furnace under a selenium atmosphere. The polymeric layer obtained by spin-coating formed interfacial dipoles which contributed to enhance the V_{oc} from 243 mV to 344 mV, and a PCE of 2.41% was obtained.

In Table 2, the ETL, HTL, and their effects on the solar cells' parameters are summarized.

Table 2. Different materials used as ETL/HTL for Sb_2Se_3 solar cells and their performance.

ETL	HTL	PCE	Absorber Deposition Method	Reference
CdS:Al	/	8.41%	RF-MS + selenization	[67]
Sb-CdS	SpirOmetad	6.13%	RTE	[68]
Cd(S,O)	/	5.76%	Thermal evaporation	[69]
CdS:O	$MoSe_2$	7.69%	CSS	[70]
CdS/SnO_2	SpirOmetad	8%	Hydrothermal	[72]
CdZnS	/	6.71%	CSS	[73]
CdS	/	5.08%	CSS	[73]
SnO_2	P3HT	4.76%	CSS	[74]
CdS/TiO_2/SnO_2	/	7%	VTD	[40]
CdS/TiO_2	/	5.82%	VTD	[80]
SnO_2	/	4.03%	VTD	[75]
La-SnO_2	/	3.25%	RTE	[76]
TiO_2 ($CdCl_2$ treatment)	SpirOmetad	6.06%	Thermal evaporation	[77]
MoO_3	CdS	6.3%	RTE	[79] Figure 8
ZTO	/	3.44%	Magnetron cosputtering	[81]
$InCl_2$–In_2S_3	SpirOmetad	5.0%	VTE	[82]
C60	NPB	5.03%	VTE	[83]
CdS	CuSCN	7.5%	VTD	[85]
CdS	WO_{3-x}/	7.1%	CSS	[86]
CdS/TiO_2	$MoSe_2$	9.2%	CSS	[25] Figure 5b
CdS	$MoSe_2$	10.12%	IVD	[29] Figure 2d
CdS:O	/	7%	CSS	[71]
CeO_2	/	5.14%	RTE	[78]
CdS	NiO_x	6.5%	VTD	[87]
SnO_2/CdS	t-Se	7.45%	CSS	[34]
CdS	MoS_3	6.65%	TE	[88]
CdS	MoO_2	8.14%	RF-MS + selenization	[89]
CdS	$CuSbSe_2$	5.87%	VTD	[90]

Table 2. *Cont.*

ETL	HTL	PCE	Absorber Deposition Method	Reference
CdS	Mo/PbSe	8.4%	CSS	[91]
TiO_2	PCDTBT	6.6%	CSS	[92]
TiO_2	P3HT	6.88%	CSS	[93]
CdS	SpirOmetad	7.27%	VTD	[94]

3.2.2. HTLs

Many hole transport layer (HTL) materials, both inorganic and organic, have been investigated and are still being explored for Sb_2Se_3 solar cells. Inorganic HTLs have the advantage of being stable and generally having higher carrier mobilities, while organic HTLs can be easily processed by printing (inkjet, roll-to-roll) in flexible organic PV.

Y. Cao et al. [95] theoretically studied inorganic hole transport materials such as Cu_2O, CuI, and NiO for Ag/ETL/Sb_2Se_3/HTL/ITO/glass architectures. With the proper absorber thickness, HTL acceptor concentration, and hole mobility, NiO as an HTL and PCBM as an ETL, the authors calculated a theoretical 24.7% efficient device.

A. Sunny et al. [96] proposed an Al/FTO/CdS/Sb_2Se_3/SnS/Mo structure, with a SnS HTL and a CdS ETL, they calculated by 1D (SCAPS-1D) simulation software an interesting PCE of 29.89%.

S. Campbell et al. [97] theoretically studied MoO_x and NiO HTLs in Sb_2Se_3 solar cells. They observed that for CSS-grown superstrate solar cells, a NiO HTL was more adequate than MoO_x since J_{sc} was enhanced by 40% compared to reference and MoO_x-based devices. In addition, they observed that NiO layers facilitated a vertical ribbon orientation growth.

NiO_x and Ni as an HTL and alternative back contact, respectively, were investigated by J. Zhang et al. [87]. The structure with a 7 nm thick NiO_x exhibited the best PCE of 6.5%.

K. Li et al. [85] investigated CuSCN as an HTL for Sb_2Se_3 solar cells achieving a 7.5% efficiency in CuSCN/Sb_2Se_3/CdS/ITO/glass structure solar cells. In this case, the strong polarity in the Cu–C–N–S chains along the *c*-axis induced the desired vertical preferential growth. Next, moderate thermal treatments (in particular 85 °C for 10 min) of CuSCN also favored a Cu ion diffusion into Sb_2Se_3 causing a grain boundary inversion and the increase in Cu vacancies in CuSCN, thus enhancing the doping density of CuSCN.

C. Liu et al. [86] investigated spin-coated WO_{3-x} as an HTL for an Sb_2Se_3 absorber deposited by CSS, and their solar cells reached a PCE of 7.1% in Sb_2Se_3 solar cells as n-i-p devices fabricated with the structure of Au/WO_{3-x}/Sb_2Se_3/CdS/FTO/glass.

K. Shen et al. [34], as already mentioned, adopted a 2 nm thick trigonal Se (t-Se) film as HTL. They observed a higher open-circuit voltage (V_{oc}), which was attributed to the band bending at the Sb_2Se_3/t-Se interface. They also observed an increased durability of the solar cells compared to those with a Spiro-OMeTAD HTL (2% vs. 40% efficiency decrease after 40 days). This confirmed the importance of using an inorganic HTL for robust and durable Sb_2Se_3-based solar cells.

Y. Ma et al. [88] investigated the use of MoS_3 as a hole extraction and transport layer. Solar cells with the Au/MoS_3/Sb_2Se_3/CdS/FTO/glass configuration exhibited a PCE of 6.65% versus 3.89% in the absence of HTL.

J. Lin et al. [89] investigated a Mo/MoO_2 interface as HTL in a Ag/ITO/CdS/Sb_2Se_3/MoO_2/Mo/glass structure. In that case, Sb_2Se_3 was obtained by Sb precursor RF sputtering and a post-selenization of the Sb layer. The MoO_2 layer suppressed the formation of the $MoSe_2$ interface layer, contributing to the interface reaching a very high PCE of 8.14%. The MoO_2 interface layer also induced the growth of (211)-oriented Sb_2Se_3 with large grains.

Q. Cang et al. [90] exploited $CuSbSe_2$ as an HTL for a Au/$CuSbSe_2$/Sb_2Se_3/CdS/FTO solar cell, where the $CuSbSe_2$ layer was obtained by co-sputtering from Cu and Sb_2Se_3 targets; a PCE of 5.87% was obtained in comparison with 4.36% without HTL. $CuSbSe_2$ contributed to enhancing the carrier concentration and reducing the photocarrier recombination associated with the ultrathin $CuSbSe_2$ layer.

A modified HTL was studied by et al. [91] with a PbSe layer evaporated at room temperature at the solar cell back contact interface with Mo. The authors observed that PbSe simultaneously facilitated the growth of Sb_2Se_3 crystals obtained by CSS with an enhanced (hk1) orientation and hole extraction at the Sb_2Se_3/Mo interface. The effect was attributed to the reduction in deep-level traps by Pb into the Sb_2Se_3 and to the formation of a blocking barrier by PbSe, contributing to reducing the carrier recombination. An 8.4% efficient Sb_2Se_3 solar cell was achieved for Ag/AZO/ZnO/CdS/Sb_2Se_3/PbSe/Mo fabricated on a flexible polyimide film (PI) substrate.

Pasini et al. [98] investigated a Fe-S-O HTL deposited at RT by RF-MS. The solar cell structure Sb_2Se_3/ZnCdS/glass with contact strips of Fe-S-O covered by Au was reported with a PCE between 5% and 6%.

Alternatives to organic HTLs have been extensively studied for Sb_2Se_3-based solar cells, showing interesting improvements in PV performance in the last years. O. S. Hutter et al. [92] used a TiO_2 layer as ETL and poly[N-9′-heptadecanyl-2,7-carbazole-alt-5,5-(4′,7′-di-2-thienyl-2′,1′,3′- benzothiadiazole)] (PCDTBT), obtained by spin-casting, as HTL achieving an interesting 6.6% efficiency for a Au/PCDTBT/Sb_2Se_3/TiO_2/FTO/glass structure where the Sb_2Se_3 absorber was obtained by CSS and a seed layer method.

Another important organic material, P3HT, has been studied in several works as HTL [74,93]. In the case of C. H. Don et al. [93], it was deposited by spin-coating in a Au/P3HT/Sb_2Se_3/TiO_2/FTO device, achieving a PCE of 6.88%.

Spiro-OMeTAD as HTL has been employed in several works [68,72,77,82,94]. Z. Cao et al. [94] recently investigated Spiro-OMeTAD as HTL and CdS as ETL. In this case the Sb_2Se_3 absorber was fabricated by the VTD method. The authors highlighted the importance of pumping excess oxygen out of the furnace tube, removing oxygen from the CdS/Sb_2Se_3 interface to both decrease the defect concentration and enhance the (hkℓ, ℓ = 1)-oriented ribbon growth. In this way, Au/Spiro-OMeTAD/Sb_2Se_3/CdS/ITO solar cells achieved an efficiency of 7.27%.

3.3. Doping

Undoped Sb_2Se_3 generally presents a low intrinsic p-type charge carrier density ($\sim 10^{13}$ cm^{-3}), which induces a small built-in potential, and thus a limited V_{oc}. However, it is also difficult to extrinsically dope Sb_2Se_3 because the doping elements often remain located between the conductive ribbons, where they are not active, and not into the lattice [10].

On the other hand, external doping in Sb_2Se_3 has been used to passivate or suppress defects, such as V_{Se} defects or grain boundaries, especially between the ribbons. This can reduce nonradiative recombination and improve V_{oc}.

The latter is the case of Na doping that was investigated in Sb_2Se_3-based solar cells by Y. Li et al. [99]. The authors found a negligible influence on the conductivity of the Sb_2Se_3 layer, arguing that Na diffused in the film and remained inert between $(Sb_4Se_6)_n$ ribbons. W-H Li et al. investigated Sb_2Se_3 doping with PbI_2 by thermal diffusion [100]. A 1 nm thin layer of PbI_2 was deposited on an ITO/glass substrate and then an amorphous Sb_2Se_3 film was grown on it. I and Pb interdiffusion was then promoted during annealing. Pb_{Sb} defects were detected in Sb_2Se_3, and Pb acted as a p-dopant, increasing the hole concentration from 10^9 to 10^{13} cm^{-3}. The authors fabricated ITO/PbI_2-doped Al/Alq3/C60/Sb_2Se_3 solar cells which exhibited a PCE of 4.43%, in comparison with a PCE of 2.87% for the undoped Sb_2Se_3-based cells.

M. Huang et al. [101] also investigated Pb doping in Sb_2Se_3. They reached a hole concentration of 10^{16} cm^{-3} also observing that Pb doping induced shallow defects corresponding to Pb_{Sb}.

Y. Ma et al. [102] studied tellurium-doped Sb_2Se_3 to reduce deep-level defects. In particular, the authors obtained Se-rich Sb_2Se_3 layers, limiting V_{Sb} and Se_{Sb} defects. This was also observed in works where the importance of selenization, also able to tailor the Se/Sb ratio to obtain Se-rich films, was clearly highlighted [103].

Cu-doped Sb_2Se_3 was presented by G. Spaggiari et al. [104] for Sb_2Se_3 obtained by LT-PED. Cu-doped Sb_2Se_3 free-carrier concentration was estimated in the order of 10^{15} cm^{-3} and successfully increased by about two orders of magnitude with respect to the undoped Sb_2Se_3.

Y. Li et al. [105] investigated Mg and Fe doping in Sb_2Se_3. The authors found that while Mg was predominately inert to the electric properties of Sb_2Se_3, Fe produced n-type doping even if the electron-free density was still low, around 10^{13} cm^{-3}. These extrinsic defects were also associated with deep levels, which are detrimental for solar cell applications.

As already mentioned, H. Guo et al. [26] introduced KOH to the surface of Sb_2Se_3 films, improving the doping density from 10^{13} to 10^{15} cm^{-3}, which contributed to enhance the solar cell performance (PCE of 7.16%).

X. Liu et al. [106] observed that in Sb_2Se_3 material, intrinsic defect acceptors Se_{Sb} and V_{Sb} formed preferentially in Se-rich conditions, while deep donors V_{Se} and Sb_{Se} were dominant in Se-poor compounds. The authors provided an in situ compensating process with Se vapor supplied during the growth, obtaining Se-rich conditions, and producing a higher film conductivity, shallower defects, and a longer carrier lifetime.

T. D. C. Hobson et al. [107] used $MgCl_2$ to n-dope Sb_2Se_3 demonstrating that chlorine was a substitutional shallow n-dopant with 10^{16}–10^{17} cm^{-3} of doping density. Solar cells based on this n-type absorber demonstrated a PCE of 7.3%.

T. D. C. Hobson et al. [108] also obtained p doping, with a carrier density of 7.4×10^{14} cm^{-3}, introducing Sn in Sb_2Se_3 layers. Sn substitutionally replaced Sb; however, the introduced Sn atom concentration was 7×10^{18} cm^{-3}, much higher than the net carrier density, probably because of the Fermi level pinning.

Sn doping was also investigated by S. Chen et al. [109] in $(Sn_xSb_{1-x})_2Se_3$ with x ranging from 0 to 0.1. P-type doping was identified, and electrical conductivity was improved by more than three orders of magnitude in comparison with the undoped samples.

Fe-doped Sb_2Se_3 was obtained in electrodeposited samples [110], with a hole density three orders of magnitude higher than the undoped films.

H. Zhou et al. [111] explored S doping of Sb_2Se_3 nanowire arrays with a gradient of its concentration whose characteristics allowed the formation of a cascade band structure, the improvement of the charge carrier transport, and consequently the increase in the solar cell fill factor. In [112], the authors also investigated S-doped Sb_2Se_3 (obtained by an electrodeposition method) increasing the p doping of 2.17×10^{16} cm^{-3} in the undoped sample to 5.63×10^{18} cm^{-3} in the S-doped one.

Silver doping has been studied by S. Gautam et al. [113], who observed that Ag doping of Sb_2Se_3 presented a dual nature dependent on the temperature. In particular, at low temperatures, Ag showed an activation energy close to undoped material, while at higher temperatures, the activation energy decreased to 0.26 eV.

Ni doping of Sb_2Se_3 also promotes p-conduction type [114] and its effect in enhancing the broadband in photodetector based on a nanowire array has been investigated.

Bi doping of Sb_2Se_3 permitted to achieve an n-doping density of around 10^{19} cm^{-3} in samples obtained by electrodeposition [115].

S. Chen et al. [116] investigated Pt doping of Sb_2Se_3 through a Pt metallic interlayer between Sb_2Se_3 and the CdS layer. Pt generated a p-doping increase of one order of magnitude (to 3.93×10^{15} cm^{-3}) in relation to the undoped sample. The authors also observed a deep-level passivation and an oxygen contamination reduction effect of the formed $PtSe_2$ layer, which, concurrently with doping, contributed to enhance the PCE from 5.58 to 7.49% in the Ag/ITO/CdS/Sb_2Se_3:Pt/Mo/glass solar structure.

Te-doped Sb_2Se_3 film by a co-post-selenization treatment was investigated by G. Chen et al. [117]. Firstly, an RF-MS deposition method was used to obtain the Sb metallic precursors thin films, then a post-selenization doping treatment was performed in a vacuum tubular furnace with Te and Se powder sources. Te-Sb_2Se_3 thin films with a preferred (hk1) orientation was successfully obtained and the Ag/ITO/CdS/Te- Sb_2Se_3/Mo solar cell achieved a PCE of 7.61% efficiency.

4. Conclusions

In this paper, we summarized the latest research on the grain orientation, ETL and HTL configurations, and doping of planar Sb_2Se_3-based solar cells fabricated using physical deposition techniques. We focused on the relationship between the deposition conditions and the resulting photovoltaic performance.

The efficiency of Sb_2Se_3 solar cells has gradually increased in the last ten years, exceeding 10.5%. This has led to a growing interest in this material as a promising candidate for the thin-film solar cell market. Advances in fabrication methods, control of ribbon orientation, defect suppression, and passivation have certainly contributed to the rapid improvement of photovoltaic performance. However, several issues, such as V_{oc} losses associated with nonradiative recombination defects and effective external doping, remain under investigation and have not been fully resolved.

Among the deposition methods, high-rate growth processes, such as CSS, RTE, IVD, and VTD, have shown the most promising results (PCE > 9–10%) for Sb_2Se_3 absorber layers in terms of vertical ribbon alignment. This is a fundamental characteristic for obtaining a material with high conductivity. Other physical deposition techniques (PDTs), such as RFMS, which have recently achieved a PCE >8%, also appear to be very promising in terms of results and scalability. For ETLs and HTLs, new strategies in interface band alignments and inorganic (especially Cd-free) ETLs such as CeO_2, TiO_2, and SnO_2 (also combined in bi- or trilayers) and HTLs such as NiO_x, CuSCN, WO_{3-x}, and MoS_3 appear as very promising candidates for new configurations of solar cells.

Among the possible dopants for Sb_2Se_3 absorber layers, K, Cu, Sn, and Pb have been explored with some success. However, passivation, surface processes, and postdeposition treatments (chemical or thermal) are still open challenges that need to be addressed to further improve the properties of Sb_2Se_3-based devices and their power conversion efficiency (PCE).

Author Contributions: Conceptualization, R.J; methodology, R.J.; validation, G.S. and F.P.; formal analysis, R.J.; investigation, R.J.; resources, S.R.; data curation, F.P.; writing—original draft preparation, R.J.; writing—review and editing, S.R, G.S. and F.P.; visualization, G.S.; supervision, F.P.; project administration, S.R.; funding acquisition, S.R. All authors have read and agreed to the published version of the manuscript.

Funding: This research was funded by Italian Ministry of the Environment and the Energy Security: Research Fund for the Italian Electrical System (type-A call, published on G.U.R.I. n. 192 on 18 August 2022). The research was also funded by Italian Ministry of University and Research: "Ecosystem for Sustainable Transition in Emilia-Romagna" (EcosistER), funded under the National Recovery and Resilience Plan (NRRP), Mission 4 Component 2 Investment 1.5—Call for tender No. 3277 of 30 December 2021.

Institutional Review Board Statement: Not applicable.

Informed Consent Statement: Not applicable.

Data Availability Statement: Not applicable.

Acknowledgments: The authors would like to thank the financial support of Coordenação de Aperfeiçoamento de Pessoal de Nível Superior (CAPES) Project PROCAD Defesa DRI 15/2019. This study is a result of the research project "nuovi Concetti, mAteriali e tecnologie per l'iNtegrazione del fotoVoltAico negli edifici in uno scenario di generazione diffuSa" (CANVAS), funded by the Italian Ministry of the Environment and the Energy Security, through the Research Fund for the Italian Electrical System (type-A call, published on G.U.R.I. n. 192 on 18 August 2022). The work is part of the project "Ecosystem for Sustainable Transition in Emilia-Romagna" (Ecosister), funded under the National Recovery and Resilience Plan (NRRP), Mission 4 Component 2 Investment 1.5—Call for tender No. 3277 of 30 December 2021 of Italian Ministry of University and Research funded by the European Union—NextGenerationEU.

Conflicts of Interest: The authors declare no conflict of interest.

Nomenclature

Ag	Silver
$AgSbSe_2$	Silver antimony selenide
Al	Aluminum
Al_2O_3	Aluminum(III) oxide
ALD	Atomic layer deposition
Alq_3	Tris(8-hydroxyquinolinato)aluminum, $Al(C_9H_6NO)_3$
Ar	Argon
Au	Gold
AZO	Aluminum-doped zinc oxide
C60	Buckminsterfullerene
CBD	Chemical bath deposition
CBO	Conduction band offset
Cd	Cadmium
$CdCl_2$	Cadmium chloride
CdS	Cadmium sulfide
CdS:O	Oxygenated cadmium sulfide
CdTe	Cadmium telluride
CdZnS	Cadmium zinc sulfide
CeO_2	Cerium(IV) oxide
CIGS, $Cu(In,Ga)Se_2$	Copper indium gallium (di)selenide
CIGSSe	Copper indium gallium sulfur selenide
CSS	Close-space sublimation
CuI	Copper(I) iodide
$CuInSe_2$	Copper indium selenide
$CuSbSe_2$	Copper antimony selenide
CuSCN	Copper(I) thiocyanate
CZ-TA	4,4′,4″,4‴-(9-Octylcarbazole-1,3,6,8-tetrayl)tetrakis(N,N-bis (4-methoxyphenyl)aniline)
CZTS	Copper zinc tin sulfide
CZTSSe	Copper zinc tin sulfur selenide
DSSC	Dye-sensitized solar cell
ETL	Electron transport layer
Fe	Iron
FTO	Fluorine-doped tin oxide
HTL	Hole transport layer
I (hkℓ)	Net intensity measured by the experimental XRD patterns after the background subtraction.
I_0 (hkℓ)	Relative intensity of the XRD reflection with (hkℓ) Miller
ITO	Indium tin oxide
IVD	Injection vapor deposition
i-ZnO	Intrinsic zinc oxide
JCPDS	Joint Committee on Powder Diffraction Standards
J_{sc}	Short-circuit current density
J–V	Current density–voltage
K	Potassium
KOH	Potassium hydroxide
La	Lanthanum
Mg	Magnesium
$MgCl_2$	Magnesium chloride
Mo	Molybdenum
$MoSe_2$	Molybdenum(IV) selenide
MoO_3	Molybdenum trioxide
Ni	Nickel
NiO_x	Nickel oxide
NPB	N,N′-Di(1-naphthyl)-N,N′-diphenyl-(1,1′-biphenyl)-4,4′-diamine
P3HT	Poly(3-hexylthiophene-2,5-diyl)
Pb	Lead

PbI_2	Lead(II) iodide
Pb_{Sb}	Substitutional defect of lead replacing antimony site
PCE	Power conversion efficiency
PCBM	[6,6]-Phenyl-C61-butyric acid methyl ester
PCDTBT	Poly[N-9′-heptadecanyl-2,7-carbazole-alt-5,5-(4′,7′-di-2-thienyl-2′,1′,3′-benzothiadiazole]
PDT	Physical deposition techniques
PED	Pulsed electron deposition
PLD	Pulsed laser deposition
Pt	Platinum
$PtSe_2$	Platinum diselenide
PV	Photovoltaic
QDs	Quantum dots
RF-MS	Radiofrequency magnetron sputtering
RTE	Rapid thermal evaporation
S	Sulfur
$SbCl_3$	Antimony trichloride
Se	Selenium
Sb	Antimony
Sb_{Se}	Substitutional defect of antimony replacing selenium site
Se_{Sb}	Substitutional defect of selenium replacing antimony site
Sb_2Se_3	Antimony triselenide
SL	Seeding layer
SLG	Soda–lime glass
SnO_2	Tin(IV) oxide
SnS	Tin(II) sulfide
$(Sn_xSb_{1-x})_2Se_3$	Tin-doped antimony selenide
Spiro-OMeTAD	2,2′,7,7′-Tetrakis[N,N-di(4-methoxyphenyl)amino]-9,9′-spirobifluorene
SRH	Shockley–Read–Hall
TiO_2	Titanium dioxide, titanium(IV) oxide, titania
TC	Texture coefficient
t-Se	Trigonal selenium
VBO	Valence band offset
V_{oc}	Open-circuit voltage
V_{Se}	Selenium vacancies
VTE	Vacuum thermal evaporation
VTD	Vapor transport deposition
WO_{3-x}	Tungsten oxide
WS_2	Tungsten disulfide
XRD	X-ray diffraction
ZnO	Zinc oxide
ZnMgO	Zinc magnesium oxide
ZnSe	Zinc selenide
ZTO	Zinc–tin oxide

References

1. Green, M.A.; Dunlop, E.D.; Hohl-Ebinger, J.; Yoshita, M.; Kopidakis, N.; Bothe, K.; Hinken, D.; Rauer, M.; Hao, X. Solar Cell Efficiency Tables (Version 60). *Prog. Photovolt.* **2022**, *30*, 687–701. [CrossRef]
2. Chen, C.; Li, K.; Tang, J. Ten Years of Sb_2Se_3 Thin Film Solar Cells. *Sol. RRL* **2022**, *6*, 2200094. [CrossRef]
3. Vadapoo, R.; Krishnan, S.; Yilmaz, H.; Marin, C. Electronic Structure of Antimony Selenide (Sb_2Se_3) from GW Calculations. *Phys. Status Solidi B* **2011**, *248*, 700–705. [CrossRef]
4. Shockley, W.; Queisser, H.J. Detailed Balance Limit of Efficiency of *P-n* Junction Solar Cells. *J. Appl. Phys.* **1961**, *32*, 510–519. [CrossRef]
5. Zhao, Y.; Wang, S.; Li, C.; Che, B.; Chen, X.; Chen, H.; Tang, R.; Wang, X.; Chen, G.; Wang, T.; et al. Regulating Deposition Kinetics via a Novel Additive-Assisted Chemical Bath Deposition Technology Enables Fabrication of 10.57%-Efficiency Sb_2Se_3 Solar Cells. *Energy Environ. Sci.* **2022**, *15*, 5118–5128. [CrossRef]
6. Zhou, Y.; Wang, L.; Chen, S.; Qin, S.; Liu, X.; Chen, J.; Xue, D.-J.; Luo, M.; Cao, Y.; Cheng, Y.; et al. Thin-Film Sb_2Se_3 Photovoltaics with Oriented One-Dimensional Ribbons and Benign Grain Boundaries. *Nat. Photonics* **2015**, *9*, 409–415. [CrossRef]

7. Ganose, A.M.; Savory, C.N.; Scanlon, D.O. Beyond Methylammonium Lead Iodide: Prospects for the Emergent Field of Ns^2 Containing Solar Absorbers. *Chem. Commun.* **2017**, *53*, 20–44. [CrossRef] [PubMed]
8. Black, J.; Conwell, E.M.; Seigle, L.; Spencer, C.W. Electrical and Optical Properties of Some M2v−bN3vi−b Semiconductors. *J. Phys. Chem. Solids* **1957**, *2*, 240–251. [CrossRef]
9. Huang, M.; Xu, P.; Han, D.; Tang, J.; Chen, S. Complicated and Unconventional Defect Properties of the Quasi-One-Dimensional Photovoltaic Semiconductor Sb_2Se_3. *ACS Appl. Mater. Interfaces* **2019**, *11*, 15564–15572. [CrossRef]
10. Dong, J.; Liu, Y.; Wang, Z.; Zhang, Y. Boosting V_{OC} of Antimony Chalcogenide Solar Cells: A Review on Interfaces and Defects. *Nano Sel.* **2021**, *2*, 1818–1848. [CrossRef]
11. Leng, M.; Luo, M.; Chen, C.; Qin, S.; Chen, J.; Zhong, J.; Tang, J. Selenization of Sb_2Se_3 Absorber Layer: An Efficient Step to Improve Device Performance of CdS/Sb_2Se_3 Solar Cells. *Appl. Phys. Lett.* **2014**, *105*, 083905. [CrossRef]
12. Wang, Y.; Ji, S.; Shin, B. Interface Engineering of Antimony Selenide Solar Cells: A Review on the Optimization of Energy Band Alignments. *J. Phys. Energy* **2022**, *4*, 044002. [CrossRef]
13. Choi, Y.C.; Mandal, T.N.; Yang, W.S.; Lee, Y.H.; Im, S.H.; Noh, J.H.; Seok, S.I. Sb_2Se_3-Sensitized Inorganic-Organic Heterojunction Solar Cells Fabricated Using a Single-Source Precursor. *Angew. Chem.* **2014**, *126*, 1353–1357. [CrossRef]
14. Giraldo, S.; Jehl, Z.; Placidi, M.; Izquierdo-Roca, V.; Pérez-Rodríguez, A.; Saucedo, E. Progress and Perspectives of Thin Film Kesterite Photovoltaic Technology: A Critical Review. *Adv. Mater.* **2019**, *31*, 1806692. [CrossRef] [PubMed]
15. Kazmerski, L.L.; White, F.R.; Ayyagari, M.S.; Juang, Y.J.; Patterson, R.P. Growth and characterization of thin-film compound semiconductor photovoltaic heterojunctions. *J. Vac. Sci. Technol.* **1977**, *14*, 65. [CrossRef]
16. Katagiri, H.; Sasaguchi, N.; Hando, S.; Hoshino, S.; Ohashi, J.; Yokota, T. Preparation and evaluation of Cu_2ZnSnS_4 thin films by sulfurization of E B evaporated precursors. *Sol. Energy Mater. Sol. Cells* **1997**, *49*, 407. [CrossRef]
17. Liang, G.-X.; Zhang, X.-H.; Ma, H.-L.; Hu, J.-G.; Fan, B.; Luo, Z.-K.; Zheng, Z.-H.; Luo, J.-T.; Fan, P. Facile Preparation and Enhanced Photoelectrical Performance of Sb_2Se_3 Nano-Rods by Magnetron Sputtering Deposition. *Sol. Energy Mater. Sol. Cells* **2017**, *160*, 257–262. [CrossRef]
18. Tang, R.; Chen, X.-Y.; Liang, G.-X.; Su, Z.-H.; Luo, J.; Fan, P. Magnetron Sputtering Deposition and Selenization of Sb_2Se_3 Thin Film for Substrate Sb_2Se_3/CdS Solar Cells. *Surf. Coat. Technol.* **2019**, *360*, 68–72. [CrossRef]
19. Spaggiari, G.; Pattini, F.; Bersani, D.; Calestani, D.; De Iacovo, A.; Gilioli, E.; Mezzadri, F.; Sala, A.; Trevisi, G.; Rampino, S. Growth and Structural Characterization of Sb_2Se_3 Solar Cells with Vertical Sb_4Se_6 Ribbon Alignment by RF Magnetron Sputtering. *J. Phys. D Appl. Phys.* **2021**, *54*, 385502. [CrossRef]
20. Ma, C.; Guo, H.; Wang, X.; Chen, Z.; Cang, Q.; Jia, X.; Li, Y.; Yuan, N.; Ding, J. Fabrication of Sb_2Se_3 Thin Film Solar Cells by Co-Sputtering of Sb_2Se_3 and Se Targets. *Sol. Energy* **2019**, *193*, 275–282. [CrossRef]
21. Liang, G.-X.; Luo, Y.-D.; Chen, S.; Tang, R.; Zheng, Z.-H.; Li, X.-J.; Liu, X.-S.; Liu, Y.-K.; Li, Y.-F.; Chen, X.-Y.; et al. Sputtered and Selenized Sb_2Se_3 Thin-Film Solar Cells with Open-Circuit Voltage Exceeding 500 MV. *Nano Energy* **2020**, *73*, 104806. [CrossRef]
22. Alamri, S.N. The Growth of CdTe Thin Film by Close Space Sublimation System. *Phys. Status Solidi A* **2003**, *200*, 352–360. [CrossRef]
23. Guo, L.; Zhang, B.; Qin, Y.; Li, D.; Li, L.; Qian, X.; Yan, F. Tunable Quasi-One-Dimensional Ribbon Enhanced Light Absorption in Sb_2Se_3 Thin-Film Solar Cells Grown by Close-Space Sublimation. *Sol. RRL* **2018**, *2*, 1800128. [CrossRef]
24. Tao, R.; Tan, T.; Zhang, H.; Meng, Q.; Zha, G. Sb_2Se_3 Solar Cells Fabricated via Close-Space Sublimation. *J. Vac. Sci. Technol. B* **2021**, *39*, 052203. [CrossRef]
25. Li, Z.; Liang, X.; Li, G.; Liu, H.; Zhang, H.; Guo, J.; Chen, J.; Shen, K.; San, X.; Yu, W.; et al. 9.2%-Efficient Core-Shell Structured Antimony Selenide Nanorod Array Solar Cells. *Nat. Commun.* **2019**, *10*, 125. [CrossRef] [PubMed]
26. Guo, H.; Zhao, C.; Xing, Y.; Tian, H.; Yan, D.; Zhang, S.; Jia, X.; Qiu, J.; Yuan, N.; Ding, J. High-Efficiency Sb_2Se_3 Solar Cells Modified by Potassium Hydroxide. *J. Phys. Chem. Lett.* **2021**, *12*, 12352–12359. [CrossRef]
27. Chen, C.; Li, K.; Chen, S.; Wang, L.; Lu, S.; Liu, Y.; Li, D.; Song, H.; Tang, J. Efficiency Improvement of Sb_2Se_3 Solar Cells via Grain Boundary Inversion. *ACS Energy Lett.* **2018**, *3*, 2335–2341. [CrossRef]
28. Wen, X.; Chen, C.; Lu, S.; Li, K.; Kondrotas, R.; Zhao, Y.; Chen, W.; Gao, L.; Wang, C.; Zhang, J.; et al. Vapor Transport Deposition of Antimony Selenide Thin Film Solar Cells with 7.6% Efficiency. *Nat. Commun.* **2018**, *9*, 2179. [CrossRef]
29. Duan, Z.; Liang, X.; Feng, Y.; Ma, H.; Liang, B.; Wang, Y.; Luo, S.; Wang, S.; Schropp, R.E.I.; Mai, Y.; et al. Sb_2Se_3 Thin-Film Solar Cells Exceeding 10% Power Conversion Efficiency Enabled by Injection Vapor Deposition Technology. *Adv. Mater.* **2022**, *34*, 2202969. [CrossRef]
30. Yang, K.; Li, B.; Zeng, G. Sb_2Se_3 Thin Film Solar Cells Prepared by Pulsed Laser Deposition. *J. Alloys Compd.* **2020**, *821*, 153505. [CrossRef]
31. Ashfold, M.N.R.; Claeyssens, F.; Fuge, G.M.; Henley, S.J. Pulsed Laser Ablation and Deposition of Thin Films. *Chem. Soc. Rev.* **2004**, *33*, 23. [CrossRef]
32. Pattini, F.; Rampino, S.; Mezzadri, F.; Calestani, D.; Spaggiari, G.; Sidoli, M.; Delmonte, D.; Sala, A.; Gilioli, E.; Mazzer, M. Role of the Substrates in the Ribbon Orientation of Sb_2Se_3 Films Grown by Low-Temperature Pulsed Electron Deposition. *Sol. Energy Mater. Sol. Cells* **2020**, *218*, 110724. [CrossRef]
33. Pattini, F.; Bronzoni, M.; Mezzadri, F.; Bissoli, F.; Gilioli, E.; Rampino, S. Dynamics of Evaporation from $CuGaSe_2$ Targets in Pulsed Electron Deposition Technique. *J. Phys. D Appl. Phys.* **2013**, *46*, 245101. [CrossRef]

34. Shen, K.; Zhang, Y.; Wang, X.; Ou, C.; Guo, F.; Zhu, H.; Liu, C.; Gao, Y.; Schropp, R.E.I.; Li, Z.; et al. Efficient and Stable Planar n–i–p Sb_2Se_3 Solar Cells Enabled by Oriented 1D Trigonal Selenium Structures. *Adv. Sci.* **2020**, *7*, 2001013. [CrossRef]
35. Bérubé, L.P.; L'Espérance, G. A Quantitative Method of Determining the Degree of Texture of Zinc Electrodeposits. *J. Electrochem. Soc.* **1989**, *136*, 2314–2315. [CrossRef]
36. Krautmann, R.; Spalatu, N.; Gunder, R.; Abou-Ras, D.; Unold, T.; Schorr, S.; Krunks, M.; Oja Acik, I. Analysis of Grain Orientation and Defects in Sb_2Se_3 Solar Cells Fabricated by Close-Spaced Sublimation. *Sol. Energy* **2021**, *225*, 494–500. [CrossRef]
37. Spalatu, N.; Krautmann, R.; Katerski, A.; Karber, E.; Josepson, R.; Hiie, J.; Acik, I.O.; Krunks, M. Screening and Optimization of Processing Temperature for Sb_2Se_3 Thin Film Growth Protocol: Interrelation between Grain Structure, Interface Intermixing and Solar Cell Performance. *Sol. Energy Mater. Sol. Cells* **2021**, *225*, 111045. [CrossRef]
38. Zhou, J.; Meng, D.; Yang, T.; Zhang, X.; Tang, Z.; Cao, Y.; Ni, J.; Zhang, J.; Hu, Z.; Pang, J. Enhanced Charge Carrier Transport via Efficient Grain Conduction Mode for Sb_2Se_3 Solar Cell Applications. *Appl. Surf. Sci.* **2022**, *591*, 153169. [CrossRef]
39. Liang, X.; Li, Z.; San, X.; Liu, T.; Liu, Y.; Shen, K.; Wang, S.; Schropp, R.E.I.; Mai, Y. Nanoepitaxy Growth of Sb_2Se_3 Nanorod Arrays on Mixed-Oriented Transparent Conducting Oxide-Coated Glass for Efficient and Quasiomnidirectional Solar Cells. *Sol. RRL* **2022**, *6*, 2100869. [CrossRef]
40. Wang, W.; Cao, Z.; Zuo, X.; Wu, L.; Luo, J.; Zhang, Y. Double Interface Modification Promotes Efficient Sb_2Se_3 Solar Cell by Tailoring Band Alignment and Light Harvest. *J. Energy Chem.* **2022**, *70*, 191–200. [CrossRef]
41. Lin, W.-W.; Wang, N.-W.; Lan, Z.-Y.; Fu, Z.; Huang, Z.-P.; Lin, L.-M.; Ye, Q.-Y.; Chen, S.-Y.; Chen, G.-L. Construction of CdS/Sb_2Se_3 Planar Heterojunction by Full Vapor Transport Deposition. *Vacuum* **2022**, *206*, 111544. [CrossRef]
42. Tang, R.; Zheng, Z.-H.; Su, Z.-H.; Li, X.-J.; Wei, Y.-D.; Zhang, X.-H.; Fu, Y.-Q.; Luo, J.-T.; Fan, P.; Liang, G.-X. Highly Efficient and Stable Planar Heterojunction Solar Cell Based on Sputtered and Post-Selenized Sb_2Se_3 Thin Film. *Nano Energy* **2019**, *64*, 103929. [CrossRef]
43. Park, S.-N.; Kim, S.-Y.; Lee, S.-J.; Sung, S.-J.; Yang, K.-J.; Kang, J.-K.; Kim, D.-H. Controlled Synthesis of (*Hk* 1) Preferentially Oriented Sb_2Se_3 Rod Arrays by Co-Evaporation for Photovoltaic Applications. *J. Mater. Chem. A* **2019**, *7*, 25900–25907. [CrossRef]
44. Liu, C.; Pan, Z.; Shen, K.; Zheng, J.; Liang, X.; Zhu, H.; Guo, F.; Li, Z.; Schropp, R.E.I.; Mai, Y. Interpenetrating Structure for Efficient Sb_2Se_3 Nanorod Array Solar Cells Loaded with $CuInSe_2$ QDs Sensitizer. *J. Energy Chem.* **2022**, *68*, 521–528. [CrossRef]
45. Guo, C.; Liang, X.; Liu, T.; Liu, Y.; Yang, L.; Lai, W.; Schropp, R.E.I.; Song, D.; Mai, Y.; Li, Z. 1D/3D Alloying Induced Phase Transition in Light Absorbers for Highly Efficient Sb_2Se_3 Solar Cells. *Sol. RRL* **2020**, *4*, 2000054. [CrossRef]
46. Fan, P.; Chen, G.-J.; Chen, S.; Zheng, Z.-H.; Azam, M.; Ahmad, N.; Su, Z.-H.; Liang, G.-X.; Zhang, X.-H.; Chen, Z.-G. Quasi-Vertically Oriented Sb_2Se_3 Thin-Film Solar Cells with Open-Circuit Voltage Exceeding 500 MV Prepared via Close-Space Sublimation and Selenization. *ACS Appl. Mater. Interfaces* **2021**, *13*, 46671–46680. [CrossRef]
47. Amin, A.; Duan, X.; Wall, J.; Khawaja, K.A.; Xiang, W.; Li, L.; Yan, F. Heterostructured CdS Buffer Layer for Sb_2Se_3 Thin Film Solar Cell. *Sol. RRL* **2023**, *7*, 2300417. [CrossRef]
48. Pasini, S.; Spoltore, D.; Parisini, A.; Foti, G.; Marchionna, S.; Vantaggio, S.; Fornari, R.; Bosio, A. Sb_2Se_3 Polycrystalline Thin Films Grown on Different Window Layers. *Coatings* **2023**, *13*, 338. [CrossRef]
49. Kim, J.; Ji, S.; Jang, Y.; Jeong, G.; Choi, J.; Kim, D.; Nam, S.-W.; Shin, B. Importance of Fine Control of Se Flux for Improving Performances of Sb_2Se_3 Solar Cells Prepared by Vapor Transport Deposition. *Sol. RRL* **2021**, *5*, 2100327. [CrossRef]
50. Dong, S.; Sun, L.; Yue, F. Influence of Selenium Growth Condition on the Photovoltaic Conversion Efficiency of Sb_2Se_3 as the Solar Cell Absorption Layer. *J. Mater. Sci Mater. Electron.* **2022**, *33*, 10335–10342. [CrossRef]
51. Zi, W.; Mu, F.; Lu, X.; Liu, Z.; Pang, X.; Yu, Z.; Li, Y.; Zhao, Z.; Lei, B.; Cheng, N.; et al. Sputtering Al_2O_3 as an Effective Interface Layer to Improve Open-Circuit Voltage and Device Performance of Sb_2Se_3 Thin-Film Solar Cells. *Mater. Sci. Semicond. Process.* **2023**, *153*, 107185. [CrossRef]
52. Kumar, V.; Artegiani, E.; Punathil, P.; Bertoncello, M.; Meneghini, M.; Piccinelli, F.; Romeo, A. Analysis of Se Co-Evaporation and Post-Selenization for Sb_2Se_3-Based Solar Cells. *ACS Appl. Energy Mater.* **2021**, *4*, 12479–12486. [CrossRef]
53. Guo, H.; Chen, Z.; Wang, X.; Cang, Q.; Jia, X.; Ma, C.; Yuan, N.; Ding, J. Enhancement in the Efficiency of Sb_2Se_3 Thin-Film Solar Cells by Increasing Carrier Concertation and Inducing Columnar Growth of the Grains. *Sol. RRL* **2019**, *3*, 1800224. [CrossRef]
54. Liu, Y.; Liu, X.; Zhuang, Y.; Li, E.; Zhang, S.; Liu, J.; Cheng, K.; Du, Z. Nanorod Array-Induced Growth of High-Quality Sb_2Se_3 Absorber Layers for Efficient Planar Solar Cells. *J. Alloys Compd.* **2023**, *949*, 169729. [CrossRef]
55. Wen, X.; Lu, Z.; Yang, X.; Chen, C.; Washington, M.A.; Wang, G.-C.; Tang, J.; Zhao, Q.; Lu, T.-M. Vertically Aligned One-Dimensional Crystal-Structured Sb_2Se_3 for High-Efficiency Flexible Solar Cells via Regulating Selenization Kinetics. *ACS Appl. Mater. Interfaces* **2023**, *15*, 22251–22262. [CrossRef]
56. Rijal, S.; Li, D.-B.; Awni, R.A.; Bista, S.S.; Song, Z.; Yan, Y. Influence of Post-Selenization Temperature on the Performance of Substrate-Type Sb_2Se_3 Solar Cells. *ACS Appl. Energy Mater.* **2021**, *4*, 4313–4318. [CrossRef]
57. Yuan, C.; Zhang, L.; Liu, W.; Zhu, C. Rapid Thermal Process to Fabricate Sb_2Se_3 Thin Film for Solar Cell Application. *Sol. Energy* **2016**, *137*, 256–260. [CrossRef]
58. Caño, I.; Vidal-Fuentes, P.; Calvo-Barrio, L.; Alcobé, X.; Asensi, J.M.; Giraldo, S.; Sánchez, Y.; Jehl, Z.; Placidi, M.; Puigdollers, J.; et al. Does Sb_2Se_3 Admit Nonstoichiometric Conditions? How Modifying the Overall Se Content Affects the Structural, Optical, and Optoelectronic Properties of Sb_2Se_3 Thin Films. *ACS Appl. Mater. Interfaces* **2022**, *14*, 11222–11234. [CrossRef] [PubMed]
59. Yang, Y.; Guo, T.; Wang, D.; Xiong, X.; Li, B. Preparation and Characterization of Pulsed Laser Deposited CdSe Window Layer for Sb_2Se_3 Thin Film Solar Cell. *J. Mater. Sci Mater. Electron.* **2020**, *31*, 13947–13956. [CrossRef]

60. Shiel, H.; Hutter, O.S.; Phillips, L.J.; Swallow, J.E.N.; Jones, L.A.H.; Featherstone, T.J.; Smiles, M.J.; Thakur, P.K.; Lee, T.-L.; Dhanak, V.R.; et al. Natural Band Alignments and Band Offsets of Sb_2Se_3 Solar Cells. *ACS Appl. Energy Mater.* **2020**, *3*, 11617–11626. [CrossRef]
61. Lu, S.; Ding, H.; Hu, J.; Liu, Y.; Zhu, J.; Kondrotas, R.; Chen, C.; Tang, J. In Situ Investigation of Interfacial Properties of Sb_2Se_3 Heterojunctions. *Appl. Phys. Lett.* **2020**, *116*, 241602. [CrossRef]
62. Mavlonov, A.; Razykov, T.; Raziq, F.; Gan, J.; Chantana, J.; Kawano, Y.; Nishimura, T.; Wei, H.; Zakutayev, A.; Minemoto, T.; et al. A Review of Sb_2Se_3 Photovoltaic Absorber Materials and Thin-Film Solar Cells. *Sol. Energy* **2020**, *201*, 227–246. [CrossRef]
63. Rahman, F.; Alam Moon, M.; Hossain, M.K.; Ali, H.; Haque, D.; Kuddus, A.; Hossain, J.; Ismail, A.B. Concurrent Investigation of Antimony Chalcogenide (Sb_2Se_3 and Sb_2S_3)-Based Solar Cells with a Potential WS2 Electron Transport Layer. *Heliyon* **2022**, *8*, e12034. [CrossRef] [PubMed]
64. Ayala-Mató, F.; Vigil-Galán, O.; Seuret-Jiménez, D.; Courel, M.; Fernández, S. Evaluation of $Cd_{1-x}Zn_xS$ as Electron Transport Layer in Superstrate and Inverted Configurations of Sb_2Se_3 Solar Cells with n-i-p Structure. *Semicond. Sci. Technol.* **2021**, *36*, 015016. [CrossRef]
65. Salem, M.S.; Shaker, A.; Abouelatta, M.; Alanazi, A.; Al-Dhlan, K.A.; Almurayziq, T.S. Numerical Analysis of Hole Transport Layer-Free Antimony Selenide Solar Cells: Possible Routes for Efficiency Promotion. *Opt. Mater.* **2022**, *129*, 112473. [CrossRef]
66. Kumari, R.; Mamta, M.; Kumar, R.; Singh, Y.; Singh, V.N. 24% Efficient, Simple ZnSe/Sb_2Se_3 Heterojunction Solar Cell: An Analysis of PV Characteristics and Defects. *ACS Omega* **2023**, *8*, 1632–1642. [CrossRef]
67. Luo, Y.; Chen, G.; Chen, S.; Ahmad, N.; Azam, M.; Zheng, Z.; Su, Z.; Cathelinaud, M.; Ma, H.; Chen, Z.; et al. Carrier Transport Enhancement Mechanism in Highly Efficient Antimony Selenide Thin-Film Solar Cell. *Adv. Funct. Mater.* **2023**, *33*, 2213941. [CrossRef]
68. Cai, H.; Cao, R.; Gao, J.; Qian, C.; Che, B.; Tang, R.; Zhu, C.; Chen, T. Interfacial Engineering towards Enhanced Photovoltaic Performance of Sb_2Se_3 Solar Cell. *Adv. Funct. Mater.* **2022**, *32*, 2208243. [CrossRef]
69. Cheng, J.; Zhang, Z.; Zhao, M.; Guan, Y.; Chen, X.; Meng, X.; Tang, H.; Li, L.; Wang, S. High-Efficiency Sb_2Se_3 Thin-Film Solar Cells Based on Cd(S,O) Buffer Layers Prepared via Spin-Coating. *Mater. Chem. Phys.* **2023**, *303*, 127794. [CrossRef]
70. Liu, Y.; Li, B.; Liang, X.; Liu, T.; Wang, S.; Li, Z. Reactively Sputtered CdS:O Buffer Layers for Substrate Sb_2Se_3 Solar Cells. *J. Alloys Compd.* **2023**, *932*, 167313. [CrossRef]
71. Guo, L.; Zhang, B.; Ranjit, S.; Wall, J.; Saurav, S.; Hauser, A.J.; Xing, G.; Li, L.; Qian, X.; Yan, F. Interface Engineering via Sputtered Oxygenated CdS:O Window Layer for Highly Efficient Sb_2Se_3 Thin-Film Solar Cells with Efficiency Above 7%. *Sol. RRL* **2019**, *3*, 1900225. [CrossRef]
72. Mao, X.; Wang, C.; Bian, M.; Wan, L.; Yang, X.; Zhou, R. The Design of SnO_2-Dominated Electron Transport Layer for High-Efficiency $Sb_2(S,Se)_3$ Solar Cells. *Phys. Status Solidi A* **2022**, *219*, 2200576. [CrossRef]
73. Li, G.; Li, Z.; Liang, X.; Guo, C.; Shen, K.; Mai, Y. Improvement in Sb_2Se_3 Solar Cell Efficiency through Band Alignment Engineering at the Buffer/Absorber Interface. *ACS Appl. Mater. Interfaces* **2019**, *11*, 828–834. [CrossRef]
74. Zhou, J.; Zhang, X.; Chen, H.; Tang, Z.; Meng, D.; Chi, K.; Cai, Y.; Song, G.; Cao, Y.; Hu, Z. Dual-Function of $CdCl_2$ Treated SnO_2 in Sb_2Se_3 Solar Cells. *Appl. Surf. Sci.* **2020**, *534*, 147632. [CrossRef]
75. Wen, S.; Yin, X.; Zhang, C.; Guo, Y.; Liu, J.; Wang, E.; Zheng, C.; Que, W.; Liu, H.; Liu, W. Achievable Efficiency Improvement of Sb_2Se_3 Thin-Film Solar Cells through Interface Engineering. *Mater. Lett.* **2021**, *283*, 128770. [CrossRef]
76. Chen, Z.; Guo, H.; Ma, C.; Wang, X.; Jia, X.; Yuan, N.; Ding, J. Efficiency Improvement of Sb_2Se_3 Solar Cells Based on La-Doped SnO_2 Buffer Layer. *Sol. Energy* **2019**, *187*, 404–410. [CrossRef]
77. Wang, Y.; Tang, R.; Huang, L.; Qian, C.; Lian, W.; Zhu, C.; Chen, T. Post-Treatment of TiO_2 Film Enables High-Quality Sb_2Se_3 Film Deposition for Solar Cell Applications. *ACS Appl. Mater. Interfaces* **2022**, *14*, 33181–33190. [CrossRef]
78. Wang, X.; Guo, H.; Chen, Z.; Ma, C.; Fang, X.; Jia, X.; Yuan, N.; Ding, J. Enhancement of Sb_2Se_3 Thin-Film Solar Cell Photoelectric Properties by Addition of Interlayer CeO_2. *Sol. Energy* **2019**, *188*, 218–223. [CrossRef]
79. Zhang, J.; Guo, H.; Jia, X.; Ning, H.; Ma, C.; Wang, X.; Qiu, J.; Yuan, N.; Ding, J. Improving the Performance of Sb_2Se_3 Thin-Film Solar Cells Using n-Type MoO_3 as the Back Contact Layer. *Sol. Energy* **2021**, *214*, 231–238. [CrossRef]
80. Wang, W.; Yao, L.; Dong, J.; Wu, L.; Cao, Z.; Hui, L.; Chen, G.; Luo, J.; Zhang, Y. Interface Modification Uncovers the Potential Application of SnO_2/TiO_2 Double Electron Transport Layer in Efficient Cadmium-Free Sb_2Se_3 Devices. *Adv. Mater. Interfaces* **2022**, *9*, 2102464. [CrossRef]
81. Luo, Y.-D.; Chen, M.; Tang, R.; Azam, M.; Chen, S.; Zheng, Z.-H.; Su, Z.-H.; Fan, P.; Ma, H.-L.; Liang, G.-X.; et al. Energy Band Alignment for Cd-Free Antimony Triselenide Substrate Structured Solar Cells by Co-Sputtering ZnSnO Buffer Layer. *Sol. Energy Mater. Sol. Cells* **2022**, *240*, 111721. [CrossRef]
82. Dong, Y.; Huang, L.; Wang, H.; Peng, X.; Wang, Y.; Tang, R.; Zhu, C.; Chen, T. Zinc Chloride-Treated Indium Sulfide as Buffer Layer for Cd-Free Antimony Selenide Solar Cells. *Sol. RRL* **2023**, *7*, 2300440. [CrossRef]
83. Cheng, C.-H.; Li, M.; Song, H.-Q.; Li, W.-H.; Leng, J.; Tian, W.; Cui, R.; Zhao, C.; Jin, S.; Liu, W.; et al. Enhanced Performance of the Sb_2Se_3 Thin-Film Solar Cell by Organic Molecule-Induced Crystallization and Suppression of the Interface Recombination. *ACS Appl. Energy Mater.* **2021**, *4*, 5079–5085. [CrossRef]
84. Rovira, D.; Ros, E.; Tom, T.; Jiménez, M.; Miguel Asensi, J.; Voz, C.; López-Vidrier, J.; Puigdollers, J.; Bertomeu, J.; Saucedo, E. Polymeric Interlayer in CdS-Free ElectronSelective Contact for Sb_2Se_3 Thin-Film Solar Cells. *Int. J. Mol. Sci.* **2023**, *24*, 3088. [CrossRef] [PubMed]

85. Li, K.; Wang, S.; Chen, C.; Kondrotas, R.; Hu, M.; Lu, S.; Wang, C.; Chen, W.; Tang, J. 7.5% n–i–p Sb_2Se_3 Solar Cells with CuSCN as a Hole-Transport Layer. *J. Mater. Chem. A* **2019**, *7*, 9665–9672. [CrossRef]
86. Liu, C.; Shen, K.; Lin, D.; Cao, Y.; Qiu, S.; Zheng, J.; Bao, F.; Gao, Y.; Zhu, H.; Li, Z.; et al. Back Contact Interfacial Modification in Highly-Efficient All-Inorganic Planar n-i-p Sb_2Se_3 Solar Cells. *ACS Appl. Mater. Interfaces* **2020**, *12*, 38397–38405. [CrossRef]
87. Zhang, J.; Kondrotas, R.; Lu, S.; Wang, C.; Chen, C.; Tang, J. Alternative Back Contacts for Sb_2Se_3 Solar Cells. *Sol. Energy* **2019**, *182*, 96–101. [CrossRef]
88. Ma, Y.; Yin, Y.; Li, G.; Lian, W.; Zhang, J.; Tang, R.; Ju, H.; Chen, T. Aqueous Solution Processed MoS_3 as an Eco-Friendly Hole-Transport Layer for All-Inorganic Sb_2Se_3 Solar Cells. *Chem. Commun.* **2020**, *56*, 15173–15176. [CrossRef]
89. Lin, J.; Chen, G.; Ahmad, N.; Ishaq, M.; Chen, S.; Su, Z.; Fan, P.; Zhang, X.; Zhang, Y.; Liang, G. Back Contact Interfacial Modification Mechanism in Highly-Efficient Antimony Selenide Thin-Film Solar Cells. *J. Energy Chem.* **2023**, *80*, 256–264. [CrossRef]
90. Cang, Q.; Guo, H.; Jia, X.; Ning, H.; Ma, C.; Zhang, J.; Yuan, N.; Ding, J. Enhancement in the Efficiency of Sb_2Se_3 Solar Cells by Adding Low Lattice Mismatch $CuSbSe_2$ Hole Transport Layer. *Sol. Energy* **2020**, *199*, 19–25. [CrossRef]
91. Liang, X.; Feng, Y.; Dang, W.; Huang, H.; Wang, X.; Guo, Y.; Shen, K.; Schropp, R.E.I.; Li, Z.; Mai, Y. High-Efficiency Flexible Sb_2Se_3 Solar Cells by Back Interface and Absorber Bulk Deep-Level Trap Engineering. *ACS Energy Lett.* **2023**, *8*, 213–221. [CrossRef]
92. Hutter, O.S.; Phillips, L.J.; Durose, K.; Major, J.D. 6.6% Efficient Antimony Selenide Solar Cells Using Grain Structure Control and an Organic Contact Layer. *Sol. Energy Mater. Sol. Cells* **2018**, *188*, 177–181. [CrossRef]
93. Don, C.H.; Shalvey, T.P.; Smiles, M.J.; Thomas, L.; Phillips, L.J.; Hobson, T.D.C.; Finch, H.; Jones, L.A.H.; Swallow, J.E.N.; Fleck, N.; et al. Multi-Phase Sputtered TiO_2-Induced Current–Voltage Distortion in Sb_2Se_3 Solar Cells. *Adv. Mater. Interfaces* **2023**, *10*, 2300238. [CrossRef]
94. Cao, Z.; Wang, W.; Dong, J.; Lou, L.; Liu, H.; Wang, Z.; Luo, J.; Liu, Y.; Dai, Y.; Li, D.; et al. Oxygen Content Modulation toward Highly Efficient Sb_2Se_3 Solar Cells. *ACS Appl. Mater. Interfaces* **2022**, *14*, 55691–55699. [CrossRef]
95. Cao, Y.; Zhu, X.; Chen, H.; Zhang, X.; Zhouc, J.; Hu, Z.; Pang, J. Towards High Efficiency Inverted Sb_2Se_3 Thin Film Solar Cells. *Sol. Energy Mater. Sol. Cells* **2019**, *200*, 109945. [CrossRef]
96. Sunny, A.; Ahmed, S.R.A. Numerical Simulation and Performance Evaluation of Highly Efficient Sb_2Se_3 Solar Cell with Tin Sulfide as Hole Transport Layer. *Phys. Status Solidi B* **2021**, *258*, 2000630. [CrossRef]
97. Campbell, S.; Phillips, L.J.; Major, J.D.; Hutter, O.S.; Voyce, R.; Qu, Y.; Beattie, N.S.; Zoppi, G.; Barrioz, V. Routes to Increase Performance for Antimony Selenide Solar Cells Using Inorganic Hole Transport Layers. *Front. Chem.* **2022**, *10*, 954588. [CrossRef]
98. Pasini, S.; Spoltore, D.; Parisini, A.; Marchionna, S.; Fornasini, L.; Bersani, D.; Fornari, R.; Bosio, A. Innovative Back-Contact for Sb_2Se_3-Based Thin Film Solar Cells. *Sol. Energy* **2023**, *249*, 414–423. [CrossRef]
99. Li, Y.; Zhou, Y.; Luo, J.; Chen, W.; Yang, B.; Wen, X.; Lu, S.; Chen, C.; Zeng, K.; Song, H.; et al. The Effect of Sodium on Antimony Selenide Thin Film Solar Cells. *RSC Adv.* **2016**, *6*, 87288–87293. [CrossRef]
100. Li, W.-H.; Li, M.; Hu, Y.-J.; Cheng, C.-H.; Kan, Z.-M.; Yu, D.; Leng, J.; Jin, S.; Cong, S. Enhanced Performance of Antimony Selenide Thin Film Solar Cell Using PbI_2 as a Dopant. *Appl. Phys. Lett.* **2021**, *118*, 093903. [CrossRef]
101. Huang, M.; Lu, S.; Li, K.; Lu, Y.; Chen, C.; Tang, J.; Chen, S. P-Type Antimony Selenide via Lead Doping. *Sol. RRL* **2022**, *6*, 2100730. [CrossRef]
102. Ma, Y.; Tang, B.; Lian, W.; Wu, C.; Wang, X.; Ju, H.; Zhu, C.; Fan, F.; Chen, T. Efficient Defect Passivation of Sb_2Se_3 Film by Tellurium Doping for High Performance Solar Cells. *J. Mater. Chem. A* **2020**, *8*, 6510–6516. [CrossRef]
103. Tiwari, K.J.; Neuschitzer, M.; Espindola, M.; Sanchez, Y.; Vidal, P.; Saucedo, E.; Malar, P. Tailoring Doping of Efficient Sb_2Se_3 Solar Cells in Substrate Configuration by Low Temperature Post Deposition Selenization Process. In Proceedings of the 2018 IEEE 7th World Conference on Photovoltaic Energy Conversion (WCPEC) (A Joint Conference of 45th IEEE PVSC, 28th PVSEC & 34th EU PVSEC), Waikoloa Village, HI, USA, 10–15 June 2018; IEEE: Waikoloa Village, HI, USA, 2018; pp. 1858–1860. [CrossRef]
104. Spaggiari, G.; Bersani, D.; Calestani, D.; Gilioli, E.; Gombia, E.; Mezzadri, F.; Casappa, M.; Pattini, F.; Trevisi, G.; Rampino, S. Exploring Cu-Doping for Performance Improvement in Sb_2Se_3 Photovoltaic Solar Cells. *Int. J. Mol. Sci.* **2022**, *23*, 15529. [CrossRef] [PubMed]
105. Li, Y.; Zhou, Y.; Zhu, Y.; Chen, C.; Luo, J.; Ma, J.; Yang, B.; Wang, X.; Xia, Z.; Tang, J. Characterization of Mg and Fe Doped Sb_2Se_3 Thin Films for Photovoltaic Application. *Appl. Phys. Lett.* **2016**, *109*, 232104. [CrossRef]
106. Liu, X.; Xiao, X.; Yang, Y.; Xue, D.-J.; Li, D.-B.; Chen, C.; Lu, S.; Gao, L.; He, Y.; Beard, M.C.; et al. Enhanced Sb_2Se_3 Solar Cell Performance through Theory-Guided Defect Control: Enhanced Sb_2Se_3 Solar Cell Performance. *Prog. Photovolt. Res. Appl.* **2017**, *25*, 861–870. [CrossRef]
107. Hobson, T.D.C.; Phillips, L.J.; Hutter, O.S.; Shiel, H.; Swallow, J.E.N.; Savory, C.N.; Nayak, P.K.; Mariotti, S.; Das, B.; Bowen, L.; et al. Isotype Heterojunction Solar Cells Using N-Type Sb_2Se_3 Thin Films. *Chem. Mater.* **2020**, *32*, 2621–2630. [CrossRef]
108. Hobson, T.D.C.; Shiel, H.; Savory, C.N.; Swallow, J.E.N.; Jones, L.A.H.; Featherstone, T.J.; Smiles, M.J.; Thakur, P.K.; Lee, T.-L.; Das, B.; et al. P-Type Conductivity in Sn-Doped Sb_2Se_3. *J. Phys. Energy* **2022**, *4*, 045006. [CrossRef]
109. Chen, S.; Qiao, X.; Zheng, Z.; Cathelinaud, M.; Ma, H.; Fan, X.; Zhang, X. Enhanced Electrical Conductivity and Photoconductive Properties of Sn-Doped Sb_2Se_3 Crystals. *J. Mater. Chem. C* **2018**, *6*, 6465–6470. [CrossRef]
110. Costa, M.B.; De Souza Lucas, F.W.; Mascaro, L.H. Electrodeposition of Fe-Doped Sb_2Se_3 Thin Films for Photoelectrochemical Applications and Study of the Doping Effects on Their Properties. *J. Solid State Electrochem.* **2018**, *22*, 1557–1562. [CrossRef]

111. Zhou, H.; Feng, M.; Feng, M.; Gong, X.; Zhang, D.; Zhou, Y.; Chen, S. Gradient Doping of Sulfur in Sb_2Se_3 Nanowire Arrays as Photoelectrochemical Photocathode with a 2% Half-Cell Solar-to-Hydrogen Conversion Efficiency. *Appl. Phys. Lett.* **2020**, *116*, 113902. [CrossRef]
112. Baghbanzadeh-Dezfuli, B.; Jamali-Sheini, F.; Cheraghizade, M. Electrochemical Synthesis of S-Doped Sb_2Se_3 Nanostructures and Photo-Switching Behaviour. *Opt. Quantum Electron.* **2023**, *55*, 4. [CrossRef]
113. Gautam, S.; Thakur, A.; Tripathi, S.K.; Goyal, N. Effect of Silver Doping on the Electrical Properties of A- Sb_2Se_3. *J. Non-Cryst. Solids* **2007**, *353*, 1315–1321. [CrossRef]
114. Wu, W.; Li, Y.; Liang, L.; Hao, Q.; Zhang, J.; Liu, H.; Liu, C. Enhanced Broadband Responsivity of Ni-Doped Sb_2Se_3 Nanorod Photodetector. *J. Phys. Chem. C* **2019**, *123*, 14781–14789. [CrossRef]
115. Li, J.; Wang, B.; Liu, F.; Yang, J.; Li, J.; Liu, J.; Jia, M.; Lai, Y.; Liu, Y. Preparation and Characterization of Bi-Doped Antimony Selenide Thin Films by Electrodeposition. *Electrochim. Acta* **2011**, *56*, 8597–8602. [CrossRef]
116. Chen, S.; Luo, P.; Ren, D.-L.; Duan, C.-Y.; Ma, X.-F.; Su, Z.-H.; Zheng, Z.-H.; Fan, P.; Liang, G.-X.; Tang, R. An Effective Engineering with Simultaneous Carrier Density Enhancement and Interface Optimization Enables Efficient Sb_2Se_3 Solar Cells. *Appl. Surf. Sci.* **2023**, *619*, 156783. [CrossRef]
117. Chen, G.; Li, X.; Abbas, M.; Fu, C.; Su, Z.; Tang, R.; Chen, S.; Fan, P.; Liang, G. Tellurium Doping Inducing Defect Passivation for Highly Effective Antimony Selenide Thin Film Solar Cell. *Nanomaterials* **2023**, *13*, 1240. [CrossRef] [PubMed]